AD-A185 131 FINAL REPORT ON CONTRACT F49620-85-C-0026 VOLUME 3(U) 1/1
PRINCETON UNIV NJ DEPT OF MECHANICAL AND AEROSPACE
ENGINEERING S A ORSZAG MAY 87 AFOSR-TR-87-1349-VOL-3
UNCLASSIFIED F49620-85-C-0026 F/G 20/4 NL

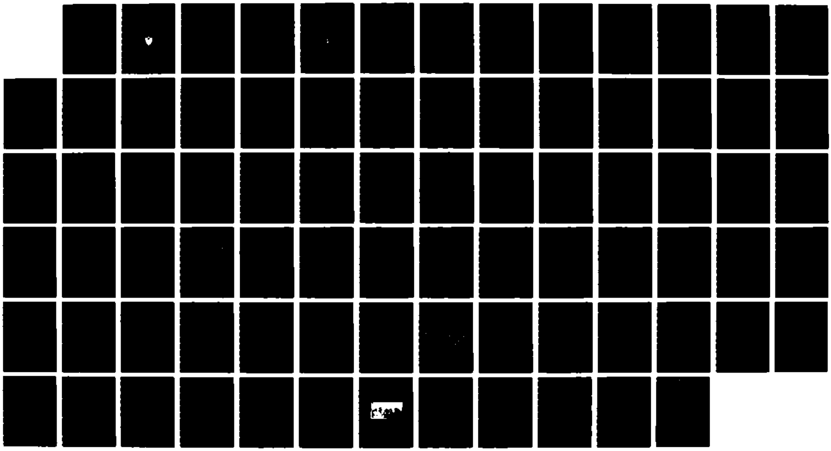

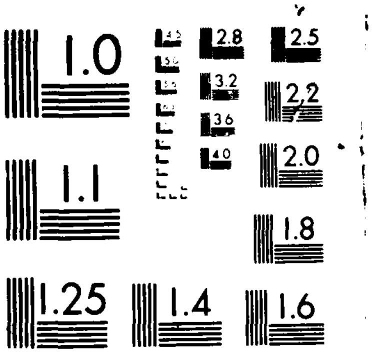
1.0
2.8
2.5
3.2
2.2
3.6
4.0
2.0
1.1
1.8
1.25
1.4
1.6

MICROCOPY RESOLUTION TEST CHART
NATIONAL BUREAU OF STANDARDS 1963 A

2

AFOSR-TR- 87-1349

DTIC FILE COPY

AD-A185 131

FINAL REPORT ON
AFOSR CONTRACT F49620-85-C-0026

Steven A. Orszag, Principal Investigator
Department of Mechanical and Aerospace Engineering
Princeton University
Princeton, NJ 08544

Volume 3

DTIC
ELECTE
SEP 30 1987
S D
D

DISTRIBUTION STATEMENT A
Approved for public release;
Distribution Unlimited

PRINCETON UNIVERSITY

87 9 24 247

UNCLASSIFIED

SECURITY CLASSIFICATION OF THIS PAGE

AD-A185 131

REPORT DOCUMENTATION PAGE

1a. REPORT SECURITY CLASSIFICATION
Unclassified

1b. RESTRICTIVE MARKINGS

2a. SECURITY CLASSIFICATION AUTHORITY

2b. DECLASSIFICATION/DOWNGRADING SCHEDULE

3. DISTRIBUTION/AVAILABILITY OF REPORT
Approved for Public Release; distribution is unlimited

4. PERFORMING ORGANIZATION REPORT NUMBER(S)

5. MONITORING ORGANIZATION REPORT NUMBER(S)
AFOSR-TR- 87-1340

6a. NAME OF PERFORMING ORGANIZATION
Princeton University

6b. OFFICE SYMBOL (If applicable)

7a. NAME OF MONITORING ORGANIZATION
AFOSR/NA

6c. ADDRESS (City, State and ZIP Code)
Princeton University
Princeton, NJ 08544

7b. ADDRESS (City, State and ZIP Code)
Building 410 Bolling AFB DC
20332-6448

8a. NAME OF FUNDING/SPONSORING ORGANIZATION
AFOSR/NA

8b. OFFICE SYMBOL (If applicable)

9. PROCUREMENT INSTRUMENT IDENTIFICATION NUMBER
F49620-85-C-0026

8c. ADDRESS (City, State and ZIP Code) Bld 410
Bolling Air Force Base
Washington, DC 20332-6448

10. SOURCE OF FUNDING NOS.

PROGRAM ELEMENT NO.	PROJECT NO.	TASK NO.	WORK UNIT NO.
61102F	2307	A2	

11. TITLE (Include Security Classification) Final Report on Contract F49620-85-C-0026 Vol. 3

12. PERSONAL AUTHOR(S)
Steven A. Orszag

13a. TYPE OF REPORT
Final Report

13b. TIME COVERED
FROM 10/1/84 TO 11/30/86

14. DATE OF REPORT (Yr., Mo., Day)
May, 1987

15. PAGE COUNT

16. SUPPLEMENTARY NOTATION

17. COSATI CODES

FIELD	GROUP	SUB. GR.

18. SUBJECT TERMS (Continue on reverse if necessary and identify by block number)
Turbulence, Numerical Simulation

19. ABSTRACT (Continue on reverse if necessary and identify by block number)

This report consists of papers that summarize work done on this research project. The major results include: 1) The development and application of the renormalization group method to the calculation of fundamental constants of turbulence, the construction of turbulence transport models, and large-eddy simulations; 2) The application of RNG methods to turbulent heat transfer through the entire range of experimentally accessible Reynolds numbers; 3) The discovery that high Reynolds number turbulent flows tend to act as if they had weak nonlinearities, at least when viewed in terms of suitable 'quasi-particles'; 4) The further analysis of secondary instability mechanisms in free shear flows, including the role of these instabilities in chaotic, 3-D free shear flows; 5) The further development of numerical simulations of turbulent spots in wall bounded shear flows; 6) The study of cellular automata for the solution of fluid mechanical problems; 7) The clarification of the relationship between the hyperscale instability of anisotropic small-scale flow structures to long-wavelength perturbations and the cellular automaton description →

20. DISTRIBUTION/AVAILABILITY OF ABSTRACT
UNCLASSIFIED/UNLIMITED ☒ SAME AS RPT. ☒ DTIC USERS ☐

21. ABSTRACT SECURITY CLASSIFICATION
Unclassified

22a. NAME OF RESPONSIBLE INDIVIDUAL
Dr James M McMichael

22b. TELEPHONE NUMBER (Include Area Code)
(202) 767-4936

22c. OFFICE SYMBOL
AFOSR/NA

DD FORM 1473, 83 APR EDITION OF 1 JAN 73 IS OBSOLETE.

SECURITY CLASSIFICATION OF THIS PAGE

UNCLASSIFIED

TRACT, continued from other side

fluids; 8) The development of efficient methods to analyze the structure of ange attractors in the description of dynamical systems; 9) The analysis of erscale instability as a mechanism for destabilization of coherent flow structures.

2

FINAL REPORT ON
AFOSR CONTRACT F49620-85-C-0026

Steven A. Orszag, Principal Investigator
Department of Mechanical and Aerospace Engineering
Princeton University
Princeton, NJ 08544

Volume 3

DTIC
S ELECTE D
SEP 3 0 1987
D

DISTRIBUTION STATEMENT A
Approved for public release;
Distribution Unlimited

SECONDARY INSTABILITY OF A TEMPORALLY GROWING MIXING LAYER

Ralph W. Metcalfe†

Steven A. Orszag††

Marc E. Brachet*

Suresh Menon†

James J. Riley**

September 1985

DTIC
COPY
INSPECTED
6

Submitted to the Journal of Fluid Mechanics

Accession For
NTIS CRA&I ☑
DTIC TAB ☐
Unannounced ☐
Justification
By
Distribution /
Availability Codes
Dist
A-1

Flow Research Company
21414-68th Avenue South
Kent, Washington 98032

---

† Flow Research Company, Kent, WA 98032

†† Applied & Computational Mathematics, Princeton University, Princeton, NJ 08544

* CNRS, Observatoire de Nice, 06-Nice, France

** Department of Mechanical Engineering, University of Washington, Seattle, WA 98195

Secondary instability of a temporally growing mixing layer

by Ralph W. Metcalfe, Steven A. Orszag, Marc E. Brachet, Suresh Menon, and James J. Riley

Flow Research Company, Kent, Washington 98032

The three-dimensional stability of two-dimensional vortical states of planar mixing layers is studied by direct numerical integration of the Navier-Stokes equations. Small-scale instabilities are shown to exist for spanwise scales at which classical linear modes are stable. These modes grow on convective time scales, extract their energy from the mean flow, and persist to moderately low Reynolds numbers. Their growth rates are comparable to the most rapidly growing inviscid instability and to the growth rates of two-dimensional subharmonic (pairing) modes. At high amplitudes, they can evolve into pairs of counter-rotating, streamwise vortices, or "ribs", in the braids, which are very similar to the structures observed in laboratory experiments. The three-dimensional modes do not appear to saturate in quasi-steady states as do the purely two-dimensional fundamental and subharmonic modes in the absence of pairing. The subsequent evolution of the flow depends on the relative amplitudes of the pairing modes. Persistent pairings can inhibit three-dimensional instability and, hence, keep the flow predominantly two-dimensional. Conversely, suppression of the pairing process can drive the three-dimensional modes to more chaotic, turbulent-like states. An analysis of high-resolution simulations of fully turbulent mixing layers confirms the existence of riblike structures and that their coherence depends strongly on the presence of the two-dimensional pairing modes.

1. Introduction

Free shear flows, like those of mixing layers and jets, differ from wall-bounded flows in that they typically have inflexional mean velocity profiles and, hence, are subject to inviscid instabilities. Thus, it may be thought that the process of transition to turbulence in free shear flows would be directly amenable to analysis. Indeed, observations by Winant & Browand (1974); Brown & Roshko (1974); Wygnanski, Oster, Fiedler & Dziomba (1979); Ho & Huang (1982); Hussain (1983a), and others show the central role played by two-dimensional dynamic processes, at least through transitional regimes, in these flows. While three-dimensional small scales are observed (Miksad 1972; Bernal, Breidenthal, Brown, Konrad & Roshko 1979), they may not necessarily destroy the large-scale two-dimensional structures (Browand & Troutt 1980). In contrast, studies of wall-bounded flows have emphasized the central role of three-dimensional effects in the breakdown to turbulence.

In this paper, we investigate the interaction between linear and nonlinear two- and three-dimensional flow states that can arise during the early stages of evolution of a temporally growing turbulent mixing layer. It is shown that certain two-dimensional, nonlinear states (coherent, spanwise vortical modes) are strongly unstable to small, three-dimensional perturbations, and that these perturbations can evolve into streamwise, counterrotating vortices similar to those observed experimentally (Bernal 1981) and modeled analytically (Pierrehumbert & Widnall 1982; Lin & Corcos 1984). We find that the two- or three-dimensional character of the mixing layer depends crucially on the initial conditions, as there is a close competition between the various modes of instability.

The approach followed here is similar to that used by Orszag & Patera (1980, 1983) in their study of secondary instabilities in wall-bounded flows. The parallel laminar flow is perturbed initially by either a linear or a finite-amplitude two-dimensional disturbance that is allowed to evolve and to saturate in a quasi-steady state. The stability of this finite-amplitude vortical state to both subharmonic (pairing) two-dimensional modes and smaller-scale three-dimensional modes is then studied by numerical solution of the full three-dimensional time-dependent Navier-Stokes equations. To relate these simulations to the evolution of a turbulent mixing layer, we also examine the interaction between the evolving two-dimensional modes in their linear and nonlinear states and a broad-band, three-dimensional background noise spectrum.

The character of the pairing instability was first explained theoretically by Kelly (1967) and numerically by Patnaik, Sherman & Corcos (1976) and Collins (1982) for stratified flows, and by Riley & Metcalfe (1980) and Pierrehumbert & Widnall (1982) for unstratified flows. The nature of the two-dimensional vortical pairing as well as a model for streamwise vortical motion have been investigated numerically and theoretically (Corcos & Sherman 1984; Corcos & Lin 1984; Lin & Corcos 1984). Experimentally, coherent pairing of large-scale vortical structures in turbulent mixing layers at high Reynolds numbers was identified by Brown & Roshko (1974). Significant secondary three-dimensional instabilities in these flows have been observed by Breidenthal (1981) and Bernal (1981). The importance of these instabilities and their sensitivity to up-stream perturbations has been demonstrated experimentally by Hussain & Zaman (1978), Oster & Wygnanski (1982), and Ho & Huang (1982) among others. There is an excellent and comprehensive review of the very extensive literature on this topic by Ho & Huerre (1984).

Pierrehumbert & Widnall (1982) examined the linear two- and three-dimensional instabilities of a spatially periodic inviscid shear layer in a study closely related to the present one. They considered the stability characteristics of the model family of two-dimensional vortex-modified mixing layers with velocity fields,

$$\begin{aligned} u &= \sinh z/[\cosh z - \rho \cos x] \\ w &= -\rho \sin x/[\cosh z - \rho \cos x] \end{aligned} \qquad (1.1)$$

(Stuart 1967) for $0 \leq \rho < 1$,† and studied subharmonic pairing instabilities and a "translative" three-dimensional instability. In contrast, we consider here both the linear and nonlinear stability characteristics of time-developing viscous shear layers. The three-dimensional secondary instability we study is both the analog of the translative instability and a generalization of the instability analyzed by Orszag & Patera (1983) for wall-bounded flows. In the nonlinear state, this instability is manifest as the streamwise, counterrotating vortices (Bernal 1981) or "ribs" (Hussain 1983a) seen in laboratory experiments.

2. Numerical methods

The Navier-Stokes equations are solved in the form

$$\frac{\partial \vec{v}}{\partial t} = \vec{v} \times \vec{\omega} - \nabla \pi + \nu \nabla^2 \vec{v} \qquad (2.1)$$

$$\nabla \cdot \vec{v} = 0 \quad , \qquad (2.2)$$

---

† Note that for $\rho << 1$, the basic flow state (1.1) is of the form $\tanh z \hat{x} + \rho \,\mathrm{Re}\,[e^{i\alpha x} \underset{\sim}{V}(z)]$. At wavenumber $\alpha = 1$, there are no fundamental two-dimensional instabilities that can compete with the subharmonic ($\alpha = 1/2$) and secondary instabilities. This flow state is an inviscid neutrally stable perturbation of the mixing layer $\tanh z \hat{x}$. In contrast, the results to be reported in §3 involve unstable fundamental perturbations to the mixing layer.

where $\vec{\omega} = \nabla \times \vec{v}$ is the vorticity and $\pi = p + 1/2\ |\vec{v}|^2$ is the pressure head. Periodic boundary conditions are applied in the streamwise, x, and spanwise, y, directions, where

$$\vec{v}(x + 4\pi/\alpha, y, z, t) = \vec{v}(x,y,z,t) \qquad (2.3)$$

$$\vec{v}(x, y + 2\pi/\beta, z, t) = \vec{v}(x,y,z,t)\ ,$$

while the flow is assumed quiescent ($\vec{v} \to U_\pm \hat{x}$; $U_\pm$ constants) as $z \to \pm\infty$. Note that the assumed periodicity length B is $4\pi/\alpha$ (or $8\pi/\alpha$) to accommodate both the fundamental mode, with x-wavenumber α, and its subharmonic, with x-wavenumber $\alpha/2$ (or $\alpha/4$).†

Our simulations are of a temporally growing mixing layer. By avoiding the requirement of imposing inflow-outflow boundary conditions, which is essential in simulations of a spatially growing flow, a faster, more efficient code can be written. Thus, the temporally evolving mixing layer can be simulated at higher Reynolds numbers and with better resolution than the spatial flow for a given level of computer resources. As will be shown later, there are very important linear and nonlinear dynamic features that are common to the two flows, so a detailed analysis of numerical simulations of a temporally growing flow can yield important insight into the evolution in the spatial case. There are also significant differences between the flows, which should be addressed by future simulations using inflow-outflow boundary conditions.

---

† Pierrehumbert & Widnall (1982) point out that Floquet theory implies that the Navier-Stokes equations linearized about a flow periodic in x admit solutions of the more general form $\vec{v}(x,y,z) = e^{i\gamma x}\,\vec{V}(x,y,z)$, where $\vec{V}$ is periodic in x with the same periodicity as the basic flow and γ is arbitrary. However, Pierrehumbert & Widnall consider only the subharmonic and fundamental cases. The analysis, which has not yet been done for more general γ, may be able to address more precisely such phenomena as the "collective interaction" described in experiments by Ho & Nosseir (1981). Indeed, Busse & Clever (1979) point out the importance of these general γ-modes in Benard convection. The present study is restricted to γ being a half-integer multiple of the fundamental wavenumber, because our code is fully nonlinear with the periodicity condition (2.3). Numerical simulations (Corcos & Sherman 1984) with values of γ different from ours indicate that the longest wave allowed by the grid will eventually dominate, although the details of the "pairing" process may differ.

We have used two independently written numerical codes for the simulations described in this paper. In the first, the dynamical equations are solved using pseudospectral methods in which the flow variables are expanded in the series

$$\vec{v}(x,y,z,t) = \sum_{|m|<\frac{1}{2}M} \sum_{|n|<\frac{1}{2}N} \sum_{p=0}^{P} \vec{u}(m,n,p,t)\, e^{im\alpha x}\, e^{in\beta y}\, T_p(Z), \qquad (2.4)$$

where n and p are integers, while m is a half-integer when one pairing is allowed and a whole integer if all pairing modes are excluded. Here $Z = f(z)$ is a transformed z-coordinate satisfying $Z = \pm 1$ when $z = \pm \infty$. Two choices of f(z) have been studied, viz.

$$Z = \tanh \frac{z}{L} \quad (|z| < \infty, \ |Z| < 1) \qquad (2.5)$$

and

$$Z = \frac{z}{\sqrt{z^2 + L^2}} \quad (|z| < \infty, \ |Z| < 1), \qquad (2.6)$$

where L is a suitable scale factor. With these mappings, derivatives with respect to z are evaluated pseudospectrally using the relations

$$\frac{\partial \vec{v}}{\partial z} = \frac{1}{L}(1 - Z^2)\frac{\partial \vec{v}}{\partial Z} \qquad (2.7)$$

$$\frac{\partial \vec{v}}{\partial z} = \frac{1}{L}\sqrt{1 - Z^2}\,\frac{\partial \vec{v}}{\partial Z} \qquad (2.8)$$

for (2.5) and (2.6), respectively.

Time stepping is done by a fractional step method in which the nonlinear terms are marched in time using a second-order Adams-Bashforth scheme while pressure head and viscous effects are imposed implicitly using Crank-Nicolson differencing. This scheme is globally second-order-accurate in time, despite time splitting (Orszag, Deville & Israeli 1985), because the various split operators commute in the case of quiescent boundary conditions at $z = \pm \infty$.

There is one further technical detail regarding this numerical method that should be discussed here. Various Poisson equations, like

$$\frac{d^2\Pi}{dz^2} - (m^2 + n^2)\,\Pi = g(z) \qquad (|z| < \infty) \ , \tag{2.9}$$

are solved by expansion in the eigenfunctions of d^2/dz^2:

$$\frac{d^2}{dz^2}\, e_k(z) = \lambda_k e_k(z) \qquad (|z| < \infty) \ . \tag{2.10}$$

Thus, if

$$g(z) = \sum_{k=0}^{P} g_k e_k(z) \ ,$$

then

$$\Pi(z) = \sum_{k=0}^{P} \frac{g_k}{\lambda_k - (m^2+n^2)}\, e_k(z) \tag{2.11}$$

We remark that this technique gives spectrally accurate solutions, despite the fact that the continuous version of the eigenvalue problem (2.10) has only a continuous, and hence singular, spectrum. Also, note that all the eigenvalues λ_k are real and nonpositive; for both mappings (2.5) and (2.6), there are precisely three zero eigenvalues λ_1, λ_2, λ_3. One of these zero eigenmodes is physical, viz. $e_1(z) = 1$, but the other two are highly oscillatory and unphysical. Indeed, since the spectral (Chebyshev) derivative of $T_p(Z)$ vanishes except at $Z = \pm 1$, $e_2(Z) = T_p(Z)$ is a zero eigenfunction of d^2/dz^2; $T_p(Z_j) = (-1)^j$ at the Chebyshev collocation points $Z_j = \cos \pi j/P$. The third zero eigenmode oscillates and grows roughly like z. When $m = n = 0$, the incompressibility constraint (2.2) requires that this mode of the z-velocity field vanish identically so there is no difficulty with the zero-pressure eigenvalues $\lambda_1, \lambda_2, \lambda_3$.

Comparisons of the behavior of linear Orr-Sommerfeld eigenmodes obtained using mappings (2.5) and (2.6) show that (2.6) gives a superior representation of these modes unless L is fine tuned, which is not convenient in the nonlinear dynamic runs.† Some representative results are given in Table 1. Notice that as α increases, the optimal choice of map scale L decreases. Also, notice that the accuracy of the eigenvalue is much more sensitive to L for the hyperbolic tangent mapping (2.5) than for (2.6).

This nonlinear, time-dependent Navier-Stokes code has been tested for the generalized Taylor-Green vortex flow (2.12) and also for linearized eigenfunction behavior, with satisfactory agreement being achieved with power series in t (Brachet et al. 1983) and linear behavior, respectively.

The second code used in the simulations is similar to the one just described, except that sine and cosine expansions in z were used instead of Chebyshev polynomials (2.4). Thus, the transverse domain extent is finite, and care must be taken to identify possible interference effects. Comparisons with results from the first simulations as well as simulations performed on varying size domains has verified that such effects are small for the cases

---

† There is one case in which it seems that the hyperbolic tangent mapping (2.5) is more convenient than the algebraic mapping (2.6). This flow is the generalized Taylor-Green vortex flow that develops from the initial conditions

$$\begin{aligned} u(x,y,z,0) &= \sin x \cos y/\cosh^2 z \\ v(x,y,z,0) &= -\cos x \sin y/\cosh^2 z \qquad (2.12) \\ w(x,y,z,0) &= 0 \quad . \end{aligned}$$

The evolution of this flow seems best studied, either by power series or initial value methods, using (2.5) with L = 1. The time evolution of this free shear flow is remarkably similar to that of the periodic Taylor-Green vortex (Brachet, Meiron, Orszag, Nickel, Morf & Frisch 1983).

presented here. Aside from details of the input/output buffering routines and the size of the arrays used in the computations, the basic code structure is similar to that described in Orszag & Pao (1974).

3. Two-dimensional instabilities

In this and the following sections, results are reported for the evolution of initial velocity fields of the form

$$\vec{v}(x,y,z,0) = U_0(z)\,\hat{x} + \mathrm{Re}\left[A_{10}\vec{v}_{10}(z)e^{i\alpha(x+\theta)} + A_{\frac{1}{2},0}\vec{v}_{\frac{1}{2},0}(z)e^{\frac{1}{2}i\alpha x} + A_{11}\vec{v}_{11}(z)e^{i\alpha(x+\phi)+i\beta y}\right], \tag{3.1}$$

where θ is the phase shift between the fundamental and subharmonic modes, and ϕ is the corresponding phase shift of the spanwise mode. The laminar mean profile is assumed to be $U_0(z) = U_0 \tanh z/\delta_i$, an approximation to the mixing layer profile, and $v_{ij}(z)$ is normalized so that $\max_z |v_{ij}(z)| = 1$. Here, δ_i is the initial mean vorticity thickness.

The initial functions $v_{ij}(z)$ are normally chosen as the most unstable eigenfunctions of the linear Orr-Sommerfeld equation for the appropriate wavenumbers given in (3.1) (Michalke 1964).† In this representation, A_{10} is the amplitude of the fundamental two-dimensional component, $A_{1/2,0}$ is the amplitude of its subharmonic or pairing mode, and A_{11} is the amplitude of the primary three-dimensional wave with a spanwise wavelength equal to that of the fundamental two-dimensional mode. Time is nondimensionalized by U_0/δ_i and space scales by δ_i. The initial conditions are typically chosen so that $A_{1/2,0}$, $A_{11} << A_{10}$, and $A_{10} = 0.25$. The Reynolds number for the undisturbed flow is $R = U_0\delta_i/\nu$.

---

†The Reynolds numbers of the flows discussed below, while modest, are much greater than that of the onset of linear instability ($R_{crit} \approx 4$), so that even the linear modes are effectively inviscid. In this case, damped modes may lie only in the continuous spectrum (Drazin & Reid 1981) and so are singular. Whenever equation (3.1) calls for such a singular contribution to the initial condition (3.1), we choose instead the flow component $w_{nm} \equiv w_{10}$ of the fundamental mode (with u_{um} and v_{nm} determined by incompressibility).

In the absence of subharmonic and three-dimensional perturbations ($A_{1/2,0} = A_{11} = 0$), the two-dimensionally perturbed flow quickly saturates to a quasi-steady state. In figure 1, a plot is given of the time evolution of the two-dimensional disturbance energy $E_{10}(t)$ for various initial amplitudes A_{10}. The value for α is taken to be 0.4446, which is the wavenumber corresponding to the largest growth rate predicted by linear theory (Michalke 1964). [The range of inviscidly unstable wavenumbers for the tanh z profile is $0 < \alpha < 1$.] Here

$$E_{mn}(t) = \int_{-\infty}^{\infty} |\vec{v}_{mn}(z,t)|^2 \, dz \quad , \tag{3.2}$$

where

$$\vec{v}_{mn}(z,t) = \sum_{p=0}^{P} \vec{u}(m,n,p,t)\, T_p(z) \tag{3.3}$$

and $\vec{u}$ is defined by (2.4). It is apparent that E_{10} saturates into a finite-amplitude vortical state on a time scale of order 10. The independence of the peak saturation amplitude to the initial excitation amplitude except for every high initial amplitudes, which is evident in figure 1, has also been observed experimentally by Freymuth (1966). If we define the growth rate σ as

$$\sigma = (dE/dt)/(2E) \quad , \tag{3.4}$$

then for linear disturbances of the form

$$\psi = \mathrm{Re}[\varphi(z)e^{i\alpha(x-ct)}] \quad , \tag{3.5}$$

we have $\sigma = \alpha c_i$. The peak growth rate of the most unstable linear mode ($\alpha = 0.4446$) is $\sigma = 0.19$. Our growth rates, which are given later in the text, should be divided by a factor of 2 for comparison with the linear results for αc_i given by Michalke (1964) to reflect the different choice of U_0.

Figure 2 is a plot of the instantaneous spanwise vorticity distribution in the developed two-dimensional flow for one of the runs shown in figure 1. Note that while rollup is occurring by $t = 8$, in the absence of a subharmonic mode, $A_{1/2,0}$, pairing does not take place, and the flow evolves into the nonlinear, quasi-equilibrium state shown in figure 2b. This absence of pairing is analogous to that artificially induced by upstream forcing in experiments by Miksad (1972), Hussain & Zaman (1978), Oster & Wygnanski (1982), Ho & Huang (1982) and others. In these experiments, the forced mode is amplified without also amplifying its subharmonic. Thus, rollup of the forced mode is achieved without pairing, creating a region in the flow characterized by large-scale, spanwise-coherent, nonpairing modes. This produces countergradient momentum fluxes, interruption in the growth of the mixing layer thickness, and a reversal in the sign of the Reynolds stresses (Riley & Metcalfe 1980). That these phenomena are also observed experimentally makes this nonlinear, quasi-equilibrium state of interest in analyzing the physics of the laboratory flows.

The saturated two-dimensional flow state discussed above can be unstable to subharmonic perturbations, $A_{1/2,0}$ in (3.1), for suitable α (Kelly 1967). In figure 3, we plot the evolution of the subharmonic perturbation energies $E_{1/2,0}(t)$ as well as the fundamental two-dimensional energy $E_{10}(t)$. Here we choose $A_{10} = 0.25$ and $A_{1/2,0} = 3\times10^{-4}$. In figure 3, the phase difference θ between the two modes is $\pi/2\alpha$, so that pairing occurs. Values of θ other than integral multiples of π result in pairing, while pairing is temporarily inhibited when θ is near $N\pi$, with N an integer. The cases $\theta = N\pi$ are anomalous, resulting in the "shredding interaction" (Patnaik *et al.* 1976) which is rarely seen experimentally.† This subharmonic instability of the saturated two-dimensional vortical states is inviscid in character, as its growth rate asymptotically approaches a finite limit as R increases. The growth rate $\sigma_{1/2,0}$ of the amplitude of the subharmonic mode is quite significant; at R = 200, $\sigma_{1/2,0} \simeq 0.1$ when $\alpha = 0.4$ while $\sigma_{1/2,0} \simeq 0.2$ for $\alpha = 0.8$. These are not significantly different from the corresponding linear inviscid growth rates of Orr-Sommerfeld modes (Michalke 1964), which are $\sigma_{1/2,0} = 0.14$ and 0.19, respectively.

The evolution of the spanwise vorticity distribution during pairing instability is shown in the contour plots in figure 4 (from Riley & Metcalfe 1980). There is strong similarity between these figures and flow visualizations of mixing layers, such as those of Winant & Browand (1974). Note that in two spatial dimensions, the lines of constant vorticity act as fluid markers much like the dye used in experiments. The evolution of the pairing process is strongly dependent on the relative initial amplitudes of the unstable modes. When $A_{1/2,0} \simeq A_{10}$, the fundamental mode rolls up first due to its higher growth rate and shorter saturation time scale. The subharmonic continues growing after the fundamental saturates, during which time the vortex cores generated by the rollup of the fundamental are merged into the subharmonic core. In this simulation (figure 4), the subharmonic mode $A_{1/2,0}$ will become saturated after about t = 24, since there is no second subharmonic mode ($A_{1/4,0}$) with which it can pair.

---

† See Riley & Metcalfe (1980) or Ho & Huerre (1984, p. 382) for additional plots and a more detailed discussion of phase differences.

Some insight into the dynamics of this process can be gained from comparing figures 4 and 5. Figure 5 is a series of velocity vector plots at the same times as those in figure 4. At t = 8, the vortical motion of the fundamental cores dominates the flow and there are four nodal points: two at the centers of the vortex cores and two stagnation points at the centers of the braids. By t = 24, the vorticity peaks corresponding to the fundamental are still present (figure 4c), although they are no longer as dynamically significant as earlier (cf. figures 5a and 5c). At this point, there are basically two nodal points in the flow: one at the center of the subharmonic core and the other in the region of high strain at the center of the braid. By t = 32, the subharmonic mode has saturated and the vortex core collapsed into a quasi-equilibrium, nonlinear state like that for the unpaired fundamental (figure 2b).

The importance of the pairing process to the dynamic evolution of the flow is clearly demonstrated by examining plots of the Reynolds stresses (figure 6). From the dynamic equation for the integrated mean kinetic energy E_M,

$$\frac{dE_M}{dt} = \int_0^{4\pi/\alpha} \frac{\partial \bar{U}}{\partial z} \overline{uw} \, dz \tag{3.6}$$

(neglecting viscous effects), it can be seen that a positive Reynolds stress implies gradient momentum transport (since $\partial \bar{U}/\partial z > 0$) and a feed of energy from the mean flow into the perturbation field, while negative Reynolds stress produces countergradient momentum flux and feeds energy from the fluctuations back into the mean. During the early stages of pairing, the Reynolds stress is predominantly positive. However, by t = 24 (figure 6c), large negative regions (denoted by dashed lines in the figures) have developed, and by t = 32 (figure 6d), the Reynolds stress has become predominantly negative. The relevance of the pairing mode is summarized in the results presented in figure 6e. Without the subharmonic pairing mode, the Reynolds stress changes sign by $t = 16$. With the subharmonic present, however, the net Reynolds stress is still positive at $t = 16$. Thus, the suppression of pairing, whether caused by forcing, as in laboratory experiments (Hussain & Zaman 1978; Oster & Wygnanski 1982; Ho & Huang 1982), or by eliminating the subharmonic mode, as in the numerical simulations, is associated with a reversal in the sign of the Reynolds stress.

This phenomenon is apparent in figure 3, in which the energy in the fundamental, E_{10}, reaches saturation by about $t = 10$. At this point, the Reynolds stress changes sign, and a countergradient momentum flux develops. In the absence of other disturbances, this flow will then evolve into an oscillatory state characterized by an alternating energy exchange between the mean flow and the perturbation fields.

In terms of turbulence models, the presence of pairing is essential to maintain the positivity of transport coefficients (such as eddy viscosity). Since the eddy viscosity, ν_{eddy}, is related to the Reynolds stress by

$$-\overline{uw} = \nu_{eddy} \frac{\partial \overline{U}}{\partial z} , \tag{3.7}$$

it follows that suppression of the pairing corresponds to a negative eddy viscosity. This suggests that accurate simulations of flows with inhibited pairing may require the direct calculation of large-scale structures.

The energetics of the pairing instability is revealing. Energy transfers to and from the subharmonic mode may be decomposed as

$$\frac{1}{2E_{\frac{1}{2},0}} \frac{dE_{\frac{1}{2},0}}{dt} \equiv \sigma_{\frac{1}{2},0} = \gamma_M + \gamma_{2D} + \gamma_\nu , \tag{3.8}$$

where γ_M involves the nonlinear interaction of the subharmonic mode with the mean flow, γ_{2D} the nonlinear interaction of the subharmonic mode and all other two-dimensional modes, and γ_ν the viscous dissipation of pairing energy. Here γ_M and γ_{2D} involve sums over nonlinear terms in the Navier-Stokes equations but are unaffected by pressure; γ_ν is proportional to the enstrophy in the subharmonic mode. In figure 7, a plot is given of these transfer terms as a function of time. It appears that the subharmonic mode extracts most of its energy from the mean flow and that there is little net energy transfer between it and the fundamental mode. In addition, its average growth rate differs little from that in the absence of the fundamental, which is $\sigma \simeq 0.14$. Thus, the presence of the saturated two-dimensional fundamental does not turn off the subharmonic mode, and the growth rate of this latter mode is close to that of the fundamental two-dimensional instability. These results imply that even a small subharmonic perturbation will quickly achieve finite amplitude after the fundamental mode saturates, unless the amplitude of the fundamental is artificially amplified by forcing. In this simulation, the subharmonic mode saturates at $t \simeq 90$ at which time the growth rate becomes negative. It should be noted here that in attempting to compare these results for growth rates of the fundamental and subharmonic modes with experiments, it is necessary to account for the dispersion of the subharmonic modes (cf., for example, figure 2b in Ho & Huerre 1984), which is present in the spatially growing but not in the temporally growing mixing layer. Also, in comparing these growth rates with those predicted by linear theory, the growth of momentum thickness of the mixing layer over the course of the simulation should be taken into consideration.

Corcos & Sherman (1984) find that the presence of the fundamental inhibits the subharmonic growth, while Pierrehumbert & Widnall (1982) find an enhancement of growth. We find that the growth rate of the subharmonic is modulated with a period related to the oscillation time scale of the nonlinear, quasi-equilibrium fundamental mode. However, the net effect on the growth of the subharmonic due to the fundamental is to decrease $\sigma_{1/2,0}$ slightly, from about 0.16 to 0.14. While these conclusions do agree with those obtained by Kelly (1967) using perturbation theory, they show that the effect is quite small.

4. Three-dimensional instabilities

The saturated two-dimensional flow is also subject to three-dimensional instabilities. While the laminar mean flow is inviscidly unstable only for $\alpha^2 + \beta^2 < 1$, the finite-amplitude two-dimensional flow can be unstable for large β at high Reynolds numbers. In figure 8, we plot the average three-dimensional growth rate σ_{3D} versus β of the three-dimensional disturbance energy,

$$E_{3D} = \sum_{m} E_{m1}(t) \quad , \qquad (4.1)$$

for various Reynolds numbers when $\alpha = 0.4$ for a three-dimensional linear perturbation to a saturated, two-dimensional quasi-equilibrium flow. Analysis of these results suggests the conjectures that, as R increases, for a fixed β, σ_{3D} approaches a finite limit (so the secondary instability discussed is inviscid in character) and that the instability turns off for

$$\beta > \beta_{crit} \approx \frac{1}{3}\sqrt{R} \quad . \qquad (4.2)$$

Although the mean flow tanh z is both viscously and inviscidly stable for $\beta > 1$, the saturated, two-dimensional disturbed flow is strongly unstable at these scales, with disturbances growing at rates near those of the inviscid two-dimensional fundamental instability, as shown in figure 9. When the two-dimensional modes saturate, the three-dimensional modes can achieve finite amplitudes on convective time scales and thereby modify significantly the later evolution of the flow.

Like the two-dimensional modes, the three-dimensional modes evolve into vortical states at large amplitudes. Typically, these are counterrotating, streamwise vortices, or "ribs", that develop in the braids between the two-dimensional vortex cores. In figure 10, we show a three-dimensional perspective plot of surfaces having a value of 50% of the peak of the sum of the absolute values of all three vorticity components. The data are from a simulation with $A_{10} = 0.22$, $A_{1/2,0} = 0$, $A_{11} = 0.003$, $R = 28$, $\alpha = 0.4446$, and $\beta = 0.8892$ at $t = 12$. The saturated, two-dimensional vortex cores are shown spanning the domain, and the two pairs of counterrotating, streamwise vortices ($\beta = 2\alpha$), which have evolved from a low-amplitude, linear perturbation, have developed in the high-strain braid region. These are very similar to the structures seen experimentally by Breidenthal (1981) and Bernal (1981) and modeled by Lin & Corcos (1984); they will be discussed in more detail in §5. In this and subsequent simulations, the choice $\phi = \pi/2$ [equation (3.1)] was made. The choice $\phi = N\pi$ appeared to produce anomalous behavior in the evolution of the ribs, somewhat analogous to the two-dimensional shredding interaction when $\theta = N\pi$.

The cutoff as $\beta \to \beta_{crit}$ (4.2) is mainly due to increasing viscous damping, as nonlinear transfers vary less rapidly with β. This point is suggested by the results plotted in figure 11, where we plot the contributions to the growth rate σ_{3D}

$$\frac{1}{2E_{3D}} \frac{dE_{3D}}{dt} \equiv \sigma_{3D} = \gamma_M + \gamma_{2D} + \gamma_\nu \quad . \tag{4.3}$$

Here γ_M involves the nonlinear interaction of the three-dimensional and mean flows, and γ_{2D} the interaction of the three-dimensional and two-dimensional energy. The jitter in the plots is due to numerical inaccuracy in the evaluation of the nonlinear transfer terms, so only the trends in the data should be considered significant. It is suggested from the data in figure 11a that, for $\beta < \beta_{crit}$, γ_ν and $\gamma_{2D} \ll \gamma_M$ asymptotically so that the three-dimensional mode derives its energy from the mean flow with the two-dimensional disturbance acting as a catalyst for this transfer.

On the other hand, the results plotted in figure 11b show that when $\beta \approx \beta_{crit}$, γ_ν is quite significant. The three-dimensional instability seems to be turned off at a large cross-stream wavenumber β by increased dissipation rather than by any significant qualitative change in nonlinear transfers from the mean and two-dimensional components.

The nature of the competition between two-dimensional pairing and three-dimensional instability is illustrated by the results plotted in figures 12 and 13. In both figures, we have plotted the results of runs with $R = 400$, $\alpha = 0.4$, and $\beta = 0.2$. Figure 12 shows the evolution of the instabilities when the initial three-dimensional perturbation is much larger than the subharmonic mode. In this case, the pairing instability is nearly unaffected by the three-dimensional instability before finite amplitudes are reached. In figure 13, the initial conditions are chosen so that the subharmonic mode perturbation is much larger than that of the three-dimensional perturbation; it seems that the pairing process and rollup inhibit the three-dimensional instability near $t = 72$, where σ_{3D} actually becomes negative. Note that the growth rate of E_{3D} is identical for the two cases (figures 12 and 13) *until* $A_{1/2,0}$ reaches finite amplitude.

5. Instability: Dependence on initial conditions

The flows that develop from the three-dimensional secondary instability do not appear to saturate in ordered states like those of the fundamental and subharmonic two-dimensional instabilities. However, the presence of additional pairing modes can significantly enhance the overall coherence of the flow. Experiments have shown that extremely low levels of forcing can generate changes in the flow of order 1 (e.g., Gutmark & Ho 1983). This has raised concerns that unintended forms of weak excitation due to natural resonances in an experimental apparatus, or pressure feedback effects, could be modifying the evolution of the flow field (Hussain 1983b). An important difference between our numerically simulated temporally growing flows and the spatially growing flows in laboratory experiments is that influences of downstream events on the earlier stages of evolution are possible in the latter but not the former.

In figure 14a, we plot results that show the effect of the absence of a subharmonic pairing mode on the evolution of the modal energies. In the absence of the subharmonic, the fundamental quickly rolls up, a process that inhibits the growth of the low-amplitude three-dimensional disturbance. Once the fundamental reaches its saturated quasi-equilibrium state ($t = 20$), the three-dimensional modes resume their rapid growth. By about $t = 50$, the three-dimensional modes dominate the flow field. The perspective plot given in figure 14b shows this domination even at later times. Further growth of the three-dimensional perturbation energy is inhibited by the collapse of the mixing layer due to the absence of the subharmonic. With the subharmonic present, the evolution of the three-dimensional modes is dramatically different. The results plotted in figure 14c are from a simulation identical to the previous one except for the inclusion of the subharmonic mode. The three-dimensional modal growth (at amplitudes in the linear range) is now slowed both by the fundamental rollup ($t \approx 5-10$) and by the subharmonic pairing ($t \approx 20-35$). Thus, the flow is more coherent than in the absence of the subharmonic (compare figures 14b and 14d). Once the subharmonic reaches its saturated state ($t \approx 35$), the three-dimensional growth rate increases substantially.

As was pointed out in §4, the two-dimensional and three-dimensional unstable modes grow at very similar rates when all disturbance amplitudes are in the linear range. In figure 15, we plot the results of a simulation in which both fundamental and three-dimensional modes were introduced at approximately equal amplitudes, well down into the linear range. In this case, the three-dimensional mode disrupts the rollup and saturation of the fundamental mode, so that its peak amplitude is an order of magnitude smaller than without the three-dimensional mode present. As shown in figure 15b, the presence of the large three-dimensional instability substantially reduces the spanwise coherence.

To determine whether the model used to initiate the three-dimensional instabilities in the simulations described thus far was realistic, we performed several simulations initialized with a broad range of three-dimensional modes. We used an uncorrelated, random-phase velocity field having a Gaussian-shaped energy spectrum. This field was convolved with a function so that the relative turbulence intensity levels were consistent with those of experimental mixing layer data. However, the initial peak intensity level was about 3 orders of magnitude below the experimental values, so the initial disturbance growth was in the linear regime.

In figure 16a, we plot the evolution of the flow field with broad-band initial excitation. Neither fundamental nor subharmonic two-dimensional linear eigenfunction modes were explicitly included in the initial conditions, although there was energy in the corresponding wavenumbers defined by the random initialization process. Nonetheless, E_{10} and $E_{1/2,0}$ grow very rapidly initially, with $\sigma_{10} = 0.11$ and $\sigma_{1/2,0} = 0.13$ at $t = 10$ (compared with $\sigma_{1/2,0} = 0.19$ and $\sigma_{10} = 0.14$ for linear inviscid modes). E_{Σ}, which is the energy in all velocity components not having $k_y = 0$, has a growth rate of $\sigma_{3D} = 0.12$ at $t = 10$. When the modal components of E_{Σ} reach finite amplitude (at $t \approx 35$), σ_{3D} decreases sharply and the flow field is characterized by a chaotic, turbulent-like velocity field in the center of the mixing layer (figure 16b). The flow remains in this chaotic state until the subharmonic reaches nonlinear amplitude and begins to roll up. As the subharmonic reaches its saturation amplitude ($t \approx 90$), the nature of the three-dimensional velocity field evolves from a highly chaotic state to one with coherent, large-scale structures (compare figures 16b and 16c), although σ_{3D} remains approximately constant. Thus, there is a complex interaction between the two- and three-dimensional instabilities. The coherent, two-dimensional modes significantly enhance the growth of the mixing layer thickness, creating a larger region for the ultimate expansion of three-dimensional instabilities. During their rollup and pairing processes, however, the coherent, two-dimensional modes tend to reduce significantly the growth rates of the low-amplitude three-dimensional modes.

The inhibition of the three-dimensional modal growth rate by the rollup and pairing of the two-dimensional modes is a function of both the amplitude and the wavenumber of the three-dimensional modes. For low-amplitude three-dimensional modes, in the linear range, coherent rollup or pairing can actually be stabilizing. In figure 17, we plot the evolution of the modal energies as functions of time for a simulation with the same initial conditions as in figure 16 but with $A_{1/2,0} = 0.0014$. As seen in this figure, when the fundamental and subharmonic reach nonlinear amplitudes ($t \approx 25$), the three-dimensional growth is stopped completely. At higher three-dimensional modal amplitudes, however, the rollup may have little or no effect on σ_{3D}. For example, in figure 16a, σ_{3D} changes very little in the presence of the saturating subharmonic between $t = 60$ and 100. During the three-dimensional stabilization shown in figure 17, the low β modes continue to grow while the high β modes decay. This is not unreasonable, since as the scale of the mixing layer grows due to the two-dimensional pairing, the relative scale of the spanwise instability also changes. As shown in figure 8 for three-dimensional perturbations to two-dimensional saturated modes, σ_{3D} depends strongly on β. A similar effect is seen for E_{Σ} in the nonlinear range in figure 16a. This would perhaps be manifest in the formation of larger ribs after the pairing of the two-dimensional modes. One mechanism that may have a significant influence on the suppression of the three-dimensional modal growth is the temporal variation of the strain field in the braids between the coherent, two-dimensional vortices. In the early stages of rollup, a very high strain develops in the braids. This has a tendency to stretch the ribs, intensifying the streamwise vorticity. As the two-dimensional modes approach saturation, however, the strain rate decreases substantially, so that this vortex stretching mechanism is weakened.

6. The secondary instability in a turbulent flow

We have performed high-resolution (64x64x64 mode) simulations of a fully turbulent mixing layer, and it is instructive to relate the evolution of these flows to the class of instabilities discussed so far. These simulations were performed on a computational domain sufficiently large to allow two complete pairings (periodicity length $8\pi/\alpha$). The initialization procedure was similar to that discussed in §5, but the amplitudes of the initial fields were higher. Details of the numerics are given in Riley, Metcalfe & Orszag (1985).

The spanwise vorticity field after two complete pairings shows clear evidence of large-scale structures (see figures 18a and b). A comparison of the vorticity plots at two different spanwise locations indicates a strong spanwise coherence for this particular realization, although details of the structures are different. As previously noted, the secondary instabilities in the mixing layer flow are characterized by streamwise, counterrotating vortices that tend to form in the braids. Figure 19 is a contour plot of ω_x in a plane at the middle of the mixing layer ($z = 0$). The solid and dashed lines indicate positive and negative vorticity, respectively. Figure 20 is a similar plot at a streamwise location B/4 from the left boundary in figure 19. These two plots clearly indicate the presence of such vortices, although they are irregularly spaced.

One of the best laboratory visualizations of coherent, three-dimensional structures in a turbulent mixing layer was performed by Bernal & Roshko (cf. Bernal 1981). Using laser fluorescein dye techniques, they were able to illuminate the flow at a fixed streamwise location. The most striking characteristic of these photographs is the appearance of mushroom-shaped features on the braids between the two-dimensional vortex cores (figure 21a). We have been able to simulate this technique by employing a numerical code developed to study a chemically reacting mixing layer (Riley et al. 1985) in which the advection diffusion equations for a binary chemical reaction are solved along with the Navier-Stokes equations. Figure 21b is a contour plot of the concentration of one of the chemical species on the same plane as in figure 20, and figure 21c corresponds to the concentration of the other chemical species. A comparison of figures 20 and 21b shows that the counterrotating vortex pairs tend to pump fluid through the braid between their cores, increasing the reaction surface area and creating the mushroom shaped structures in the flame front, which is defined by the region of overlap between figures 21b and 21c. Such features were also noted in the model proposed by Lin & Corcos (1984).

The structure of the streamwise, counterrotating vortex tubes is made clearer by isolating the streamwise vorticity component of the flow. Figure 22 is a three-dimensional perspective plot of surfaces at which $|\omega_x|$ equals 50% of its peak value. This figure was from the same realization and at the same time as figures 18-21. The large-scale, spanwise-coherent structures do not show up in this plot since they consist mainly of spanwise vorticity, ω_y. Comparison with figures 18a and 18b shows that the ribs do form on the braid between the large-scale two-dimensional vortex cores. This structure is consistent with the model proposed by Bernal (1981) although the irregular spacing of the ribs suggests that the modification of this model proposed by Hussain (1983a) is more realistic. The effect of increased coherence of the two-dimensional pairing modes on the rib structure is shown in figure 23, which is from a simulation like the previous one but to which two-dimensional modes have been added in the initial conditions: $A_{10} = 0.1$, $A_{1/2,0} = 0.06$, $A_{1/4,0} = 0.025$ [equation (3.1)]. The resulting ribs are more coherent and more aligned in the streamwise direction. As was the case with the simulation in figure 16, the presence of the pairing mode tends to increase the coherence of the three-dimensional perturbation field.

The extreme sensitivity of the ribs to the initial or upstream flow conditions makes direct quantitative comparisons between the simulations and laboratory experiments difficult. In the simulations we have performed so far, there have been significant variations in the amplitudes and spanwise spacing of the ribs. Likewise, in the experiments of Bernal (1981), there was substantial scatter in the measurements of the rib spacing. In addition, he found that the spanwise position of the ribs appeared to be related to disturbances originating upstream in the settling chamber. Our stability analysis (figure 8) has shown that there is a broad range of spanwise wavenumbers that are unstable. Some representative values for the simulation shown in figures 18-22 are as follows: the peak spanwise vorticity normalized by the peak mean velocity gradient is about 2, while the peak streamwise vorticity is slightly higher, about 3. The spanwise vorticity amplitudes are consistent with filtered experimental data (Metcalfe, Hussain & Menon 1985), while the streamwise vorticity amplitudes are somewhat higher than in other runs. The rib spacing (estimated from figure 19) is about the same as the wavelength of the most unstable fundamental two-dimensional mode. This is in the range of values reported by Bernal (1981). A more detailed analysis of these simulations, using experimental data to refine these comparisons, is now in progress.

7. Discussion

We have shown that small-scale three-dimensional instabilities like those previously studied by Orszag & Patera (1980, 1983) and Pierrehumbert & Widnall (1982) exist in free shear flows and that these instabilities persist to moderately low Reynolds numbers. It is now clear that these modes can be responsible for the initial development of three-dimensionality in these shear flows. The dynamics of these three-dimensional instabilities is similar to that of the three-dimensional instabilities in wall-bounded shear flows. At high amplitudes, these instabilities manifest themselves mainly as counter-rotating, streamwise vortices, or ribs, that form on the braids between the spanwise-coherent, two-dimensional pairing modes; they are responsible for the generation of the mushroom-shaped features seen in laboratory experimental visualizations (Bernal 1981). While the instabilities share some features of a classical inflectional instability, including phase locking with the fundamental vortex, inflectional instabilities are preferentially two-dimensional, whereas the present instabilities are not.

The rollup and pairing of the two-dimensional modes has a stabilizing effect on the higher spanwise modes and on the overall three-dimensional growth rate when the amplitude of the three-dimensional modes is small, while the absence of pairing (saturation) can enhance the three-dimensional growth rate. However, in the absence of pairing or rollup, the three-dimensional instabilities can reach a chaotic, saturated state from which significant further growth is not possible without additional pairing. The suppression of the low-amplitude three-dimensional instabilities by pairing could explain the strong two-dimensionality of the flow near the splitter plate in many laboratory experiments. Once the three-dimensional modes reach a finite amplitude and/or the Reynolds number increases with downstream distance, the growth suppression effect is reduced, and the flow becomes more three-dimensional. Mixing can be enhanced initially by coherent forcing of the mixing layer to saturation (Hussain & Zaman 1978; Oster & Wygnanski 1982; Ho & Huang 1982), which will enhance the growth of the three-dimensional modes to a chaotic state. But this is done at the expense of reducing the growth of the mixing layer momentum thickness, which is due primarily to the pairing process. Thus, the maximization of product formation in a reacting mixing layer will require balancing the increases in the flame front area generated by the chaotic three-dimensional flow with the increases due to the more rapid mixing layer growth caused by the presence of additional pairing modes.

The results of these simulations suggest that, with respect to the growth of three-dimensional disturbances, there are several important flow states possible in an evolving mixing layer. First, there is pairing and rollup of the two-dimensional modes, which is characterized by a suppression of low-amplitude three-dimensional modal growth at low Reynolds numbers. Second, there is the saturated, two-dimensional, quasi-equilibrium, non-pairing state, which is highly unstable to three-dimensional perturbations. Finally, there are chaotic, three-dimensional states characterized by a lack of spanwise coherence from which only moderate three-dimensional growth can occur. It is from these states that more rapidly growing, large-scale, two-dimensional modes can eventually emerge and reorganize the flow in a manner consistent with that suggested by Staquet & Lesieur (1986).

It seems that the mechanics of transition in the free shear flows studied here may, in a sense, be rather more complicated than in the case of wall-bounded shear flows. In the latter case, linear instabilities are often viscously driven and, therefore, weak, so they cannot be directly responsible for the rapid distortions characteristic of transition. On the other hand, free shear flows are subject to a variety of inviscid instabilities, so there may be many paths to turbulence. We have shown that the choice of paths in any individual flow may depend on the results of competition between fundamental, subharmonic, and three-dimensional instabilities, all of which are convectively driven and, therefore, strong with comparable growth rates. Thus, the evolution of free shear flows in transitional regimes depends significantly on the past history of the flow, including the relative amplitudes of all competing modes, the mechanism of their generation, and the external environment in which the flow is embedded.

References

Bernal, L. P. 1981 The coherent structure of turbulent mixing layers. I. Similarity of the primary vortex structure. II. Secondary streamwise vortex structure. Ph.D. thesis, Calif. Inst. Technol., Pasadena.

Bernal, L. P., Breidenthal, R. E. Brown, G. L., Konrad, J. H. & Roshko, A. 1979 On the development of three dimensional small scales in turbulent mixing layers. In Proc. 2nd Int. Symp. on Turbulent Shear Flows, Imperial College, London.

Brachet, M. E., Meiron, D. I., Orszag, S. A., Nickel, B. G., Morf, R. H. & Frisch, U. 1983 Small-scale structure of the Taylor-Green vortex. J. Fluid Mech. 130, 411-452.

Breidenthal, R. 1981 Structure in turbulent mixing layers and wakes using a chemical reaction. J. Fluid Mech. 109, 1-24.

Browand, F. K. & Troutt, T. 1980 A note on spanwise structure in the two-dimensional mixing layer. J. Fluid Mech. 97, 771-781.

Brown, G. L. & Roshko, A. 1974 On density effects and large structures in turbulent mixing layers. J. Fluid Mech. 64, 775-816.

Busse, F. H. & Clever, R. M. 1979 Instabilities of convection rolls in a fluid of moderate Prandtl number. J. Fluid Mech. 91, 319-335.

Collins, D. A. 1982 A numerical study of the stability of a stratified mixing layer. Ph.D. Thesis, Department of Mathematics, McGill Univ., Montreal.

Corcos, G. M. & Sherman, F. S. 1984 The mixing layer: deterministic models of a turbulent flow. Part 1. Introduction and the two-dimensional flow. J. Fluid Mech. 139, 29-65.

Corcos, G. M. & Lin, S. J. 1984 The mixing layer: deterministic models of a turbulent flow. Part 2. The origin of the three-dimensional motion. *J. Fluid Mech.* *139*, 67-95.

Drazin, P. G. & Reid, W. H. 1981 *Hydrodynamic Stability*, Cambridge University Press.

Freymuth, P. 1966 On transition in a separated laminar boundary layer. *J. Fluid Mech.* *25*, 683-704.

Gutmark, E. & Ho, C.-M. 1983 Preferred modes and the spreading rates of jets. *Phys. Fluids* *26*, 2932-2938.

Ho, C.-M. & Huang, L.-S. 1982 Subharmonics and vortex merging in mixing layers. *J. Fluid Mech.* *119*, 443-473.

Ho, C.-M. & Huerre, P. 1984 Perturbed free shear layers. *Ann. Rev. Fluid Mech.* *16*, 365-424.

Ho, C. M. & Nosseir, N. S. 1981 Dynamics of an impinging jet. Part 1. The feedback phenomenon. *J. Fluid Mech.* *105*, 119-142.

Hussain, A. K. M. F. 1983a *Turbulence and Chaotic Phenomena in Fluids*, edited by T. Tatsumi, 453. North-Holland.

Hussain, A. K. M. F. 1983b Coherent structures--reality and myth. *Phys. Fluids* *26* (10), 2816-2850.

Hussain, A. K. M. F. & Zaman, K. B. M. Q. 1978 The free shear layer tone phenomenon and probe interference. *J. Fluid Mech.* *87*, 349-383.

Kelly, R. E. 1967 On the stability of an inviscid shear layer which is periodic in space and time. *J. Fluid Mech.* *27*, 657-689.

Lin, S. J. & Corcos, G. M. 1984 The mixing layer: deterministic models of a turbulent flow. Part 3. The effect of plane strain on the dynamics of streamwise vortices. *J. Fluid Mech.* *141*, 139-178.

Metcalfe, R. W., Hussain, A. K. M. F. & Menon, S. 1985 Coherent structures in a turbulent mixing layer: A comparison between direct numerical simulations and experiments. To appear in *Proc. 5th Symp. Turbulent Shear Flows*. Springer-Verlag.

Michalke, A. 1964 On the inviscid instability of the hyperbolic tangent velocity profile. *J. Fluid Mech.* *19*, 543-556.

Miksad, R. W. 1972 Experiments on the nonlinear stages of free shear layer transition. *J. Fluid Mech.* *56*, 695-719.

Orszag, S. A. & Pao, Y. 1974 Numerical computation of turbulent shear flows. In *Advances in Geophysics*, Vol. 18A, 225-236. Academic.

Orszag, S. A. & Patera, A. T. 1980 Subcritical transition to turbulence in plane channel flows. *Phys. Rev. Lett.* *45*, 989.

Orszag, S. A. & Patera, A. T. 1983 Secondary instability of wall-bounded shear flows. *J. Fluid Mech.* *128*, 347-385.

Orszag, S. A., Deville, M. O. & Israeli, M. 1986 Splitting methods for incompressible flow problems. *J. Comp. Phys.*, To be published.

Oster, D. & Wygnanski, I. 1982 The forced mixing layer between parallel streams. *J. Fluid Mech.* *123*, 91-130.

Patnaik, P. C., Sherman, F. S. & Corcos, G. M. 1976 A numerical simulation of Kelvin-Helmholtz waves of finite amplitude. *J. Fluid Mech.* *73*, 215-240.

Pierrehumbert, R. T. & Widnall, S. E. 1982 The two- and three-dimensional instabilities of a spatially periodic shear layer. *J. Fluid Mech.* *114*, 59-82.

Riley, J. J. & Metcalfe, R. W. 1980 Direct numerical simulation of a perturbed, turbulent mixing layer. AIAA Paper No. 80-274.

Riley, J. J., Metcalfe, R. W. & Orszag, S. A. 1985 Direct numerical simulations of chemically reacting turbulent mixing layers. Accepted for publication in *Phys. Fluids*.

Staquet, C. & Lesieur, M. 1986 The mixing layer and its coherence examined from the point of view of two-dimensional turbulence. Submitted to *J. Fluid Mech.*, September 1985.

Stuart, J. T. 1967 On finite amplitude oscillations in laminar mixing layers. *J. Fluid Mech.* *29*, 417-440.

Winant, C. D. & Browand, F. K. 1974 Vortex pairing: the mechanism of turbulent mixing-layer growth at moderate Reynolds number. *J. Fluid Mech.* *63*, 237-255.

Wygnanski, I., Oster, D., Fiedler, H. & Dziomba, B. 1979 On the perseverance of a quasi-two-dimensional eddy-structure in a turbulent mixing layer. *J. Fluid Mech.* *93*, 325-335.

Table 1. Growth rates (Im c) of the Orr-Sommerfeld eigenfunctions for the mixing layer $U_0(z) = U_0 \tanh (z/\delta_i)$†

	x-wavenumber α								
	0.25			0.5			0.75		
	Number of Chebyshev Polynomials (P+1)								
L	17	33	65	17	33	65	17	33	65
	Hyperbolic Map (2.5)								
0.5	1.534	1.375	1.238	0.579	0.501	0.457	0.160	0.150	0.150
1	0.959	0.820	0.746	0.383	0.360	0.351	0.141	0.138	0.137
2	0.635	0.614	0.605	0.344	0.342	0.342	0.137	0.137	0.137
4	0.612	0.598	0.597	0.324	0.342	0.342	0.041	0.136	0.137
8	0.539	0.597	0.597	0.115	0.322	0.342	S	0.045	0.136
16	0.202	0.526	0.596	S††	S	0.321	S	S	0.046
	Algebraic Map (2.6)								
0.5	0.699	0.588	0.599	0.345	0.346	0.342	0.131	0.138	0.137
1	0.591	0.599	0.597	0.344	0.342	0.342	0.137	0.137	0.137
2	0.600	0.597	0.597	0.342	0.342	0.342	0.136	0.137	0.137
4	0.597	0.597	0.597	0.325	0.342	0.342	0.371	0.136	0.137
8	0.542	0.597	0.597	0.009	0.322	0.342	S	0.043	0.136

---

† Here the Reynolds number is $U_0\delta_i/\nu = 100$ and the eigenvalue is the complex wave speed c for a temporal mode of the form $\psi(z)e^{i\alpha(x-ct)}$. For the most rapidly growing mode listed here, Re(c) = 0.

†† S indicates that all modes are stable with the indicated parameter values.

Figure Captions

FIGURE 1. A plot of $E_{10}(t)$ versus t for runs with $A_{1/2,0} = A_{11} = 0$ and $A_{10} = 0.5, 0.25, 0.125, 0.01$. Here the Reynolds number is $R = 400$, the spectral cutoffs in (2.4) are $M = 8$, $N = 1$, $P = 32$ (resolution 8x1x32 with no subharmonic modes), the x-wavenumber is $\alpha = 0.4$, and the time step is $\Delta t = 0.02$. Note that the flow saturates into a vortical state nearly independent of the initial perturbation. Before such saturation occurs, the perturbation grows linearly like an Orr-Sommerfeld eigenfunction.

FIGURE 2. Contour plots of spanwise (y) vorticity for the mixing layer at $t = 8$ and $t = 32$ with $R = 83$, $A_{1/2,0} = 0$, $A_{10} = 0.2$, $M = P = 64$, and $N = 1$.

FIGURE 3. Plots of the evolution of $E_{10}(t)$ and the two-dimensional subharmonic mode energy $E_{1/2,0}(t)$. Here $R = 400$, $A_{10} = 0.25$, $A_{1/2,0} = 3\text{x}10^{-4}$, $M = 8$, $N = 1$, $P = 32$, $\alpha = 0.5$, $\Delta t = 0.02$, and $\theta = \pi/2\alpha$ (phase difference between the two modes).

FIGURE 4. Spanwise vorticity contours at $t = 0, 8, 16$, and 24, during a vortex pairing run with $R = 83$, $A_{10} = 0.20$, $A_{1/2,0} = 0.14$, $M = 64$, $N = 1$, $P = 64$ (resolution 64x1x64), $\alpha = 0.4446$, $\Delta t = 0.05$, and $\theta = \pi/2\alpha$.

FIGURE 5. Velocity vector plots of the vortex pairing run shown in figure 4.

FIGURE 6. (a - d) Plots of the Reynolds stress at different times for the runs with both fundamental and subharmonic present (figure 4). (e) A plot of the Reynolds stress with and without pairing at different times.

FIGURE 7. A plot of the components γ_M, γ_{2D}, γ_V [see (3.3)] of the growth rate $\sigma_{1/2,0}$ of the subharmonic mode amplitude as functions of time for a run with $R = 200$, $A_{10} = 0.25$, $A_{1/2,0} = 3\times10^{-5}$, $M = 16$, $N = 1$, $P = 32$, $\alpha = 0.43$, and $\Delta t = 0.01$.

FIGURE 8. A plot of the computed three-dimensional growth rate σ_{3D} [see (4.3)] as a function of the spanwise wavenumber β for various Reynolds numbers. Here $\alpha = 0.4$.

FIGURE 9. A plot of the computed subharmonic growth rate $\sigma_{1/2,0}$ and three-dimensional growth rate σ_{3D} as a function of α at $R = 400$ and $\beta = 0.8$.

FIGURE 10. A three-dimensional perspective plot of surfaces having a value equal to 50% of the peak of the sum of the absolute values of all three vorticity components for a run with $R = 56$ (at $t = 12$), $M = N = P = 64$, $\alpha = 0.4446$, $\Delta t = 0.05$, $A_{10} = 0.22$, $A_{1/2,0} = 0$, $A_{11} = 0.003$, $\beta = 0.8892$ at $t = 12$.

FIGURE 11. A plot of the components γ_M, γ_{2D}, γ_V [see (4.3)] of the three-dimensional growth rate σ_{3D} as functions of time for $R = 400$, $\alpha = 0.4$, $A_{10} = 0.25$, $A_{11} = 10^{-6}$.

(a) $\beta = 4$.

(b) $\beta = 6$.

FIGURE 12. A plot of the evolution of the energies E_{10}, $E_{1/2,0}$, E_{3D} versus t for a run with $R = 400$, $\alpha = 0.4$, $\beta = 0.2$, $M = 8$, $N = 4$, $P = 32$, and initial conditions $A_{10} = 0.25$, $A_{1/2,0} = 3\times10^{-6}$, $A_{11} = 10^{-3}$. The three-dimensional mode initially dominates the subharmonic mode.

FIGURE 13. Same as figure 12, except that the initial conditions are $A_{10} = 0.25$, $A_{1/2,0} = 4\times10^{-3}$, $A_{11} = 3.3\times10^{-5}$. Here, $E_{3D}' = 10^{-3} \times E_{3D}$ from figure 12. Note that the linear growth of the three-dimensional mode is stopped when the subharmonic reaches a nonlinear amplitude.

FIGURE 14. (a) A plot of the evolution of the modal energies as functions of time. $E_S = E_{01} + E_{11} + E_{21}$, i.e., the three lowest spanwise modes with the same x-wavelength as the fundamental. $R = 100$, $\alpha = 0.4446$, $A_{10} = 0.22$, $A_{1/2,0} = 0$, and $A_{11} = 10^{-5}$.

(b) A three-dimensional perspective plot of the vorticity field as in figure 10 at $t = 96$.

(c) Same as figure 14a but $A_{1/2,0} = 0.14$.

(d) Same as figure 14b but $A_{1/2,0} = 0.14$.

FIGURE 15. (a) Same as figure 14a but $A_{10} = 10^{-3}$.

(b) Same as figure 14b but $A_{10} = 10^{-3}$ at $t = 48$.

FIGURE 16. (a) A plot of the evolution of the modal energies as functions of time. E_Σ = energy in all modes with $k_y \neq 0$. $R = 100$. Random noise initial field with peak rms velocity $\simeq 0.01$.

(b) A three-dimensional perspective plot of the vorticity field as in figure 10 at $t = 48$.

(c) Same as figure 16b but at $t = 96$.

FIGURE 17. A plot of the evolution of the modal energies as functions of time. E_Σ = energy in all modes with $k_y \neq 0$. $R = 100$, $\alpha = 0.4446$, $A_{10} = 0$, $A_{1/2,0} = 0.0014$, and $A_{11} = 10^{-5}$.

FIGURE 18. Spanwise vorticity at $y = 4\pi/\alpha$ (figure 18a) and $6\pi/\alpha$ (figure 18b). The computational domain size B is $8\pi/\alpha$. $R = 154$ and $t = 72$. Random noise initial field with peak rms velocity $\simeq 0.13$. The initial Reynolds number is $R = 28$.

FIGURE 19. Streamwise vorticity at $z = 0$ for the same run as in figure 18.

FIGURE 20. Streamwise vorticity at $x = 2\pi/\alpha$ for the same run as in figure 18.

FIGURE 21. (a) Laser sheet/fluorescein dye visualization of the braid of a turbulent mixing layer in water (from Bernal 1981).
(b) Contour plot of the species concentration field at the same time and location as in figure 20.
(c) Contour plot of the second species concentration field at the same time and location as in figure 21b.

FIGURE 22. Three-dimensional perspective plot of surfaces at which $|\omega_x|$ equals 50% of its peak value for the same run as in figure 18.

FIGURE 23. Plot of $|\omega_x|$ as in figure 22 but for a simulation to which two-dimensional modes have been added in the initial conditions: $A_{10} = 0.1$, $A_{1/2,0} = 0.06$, and $A_{1/4,0} = 0.025$ [equation (3.1)].

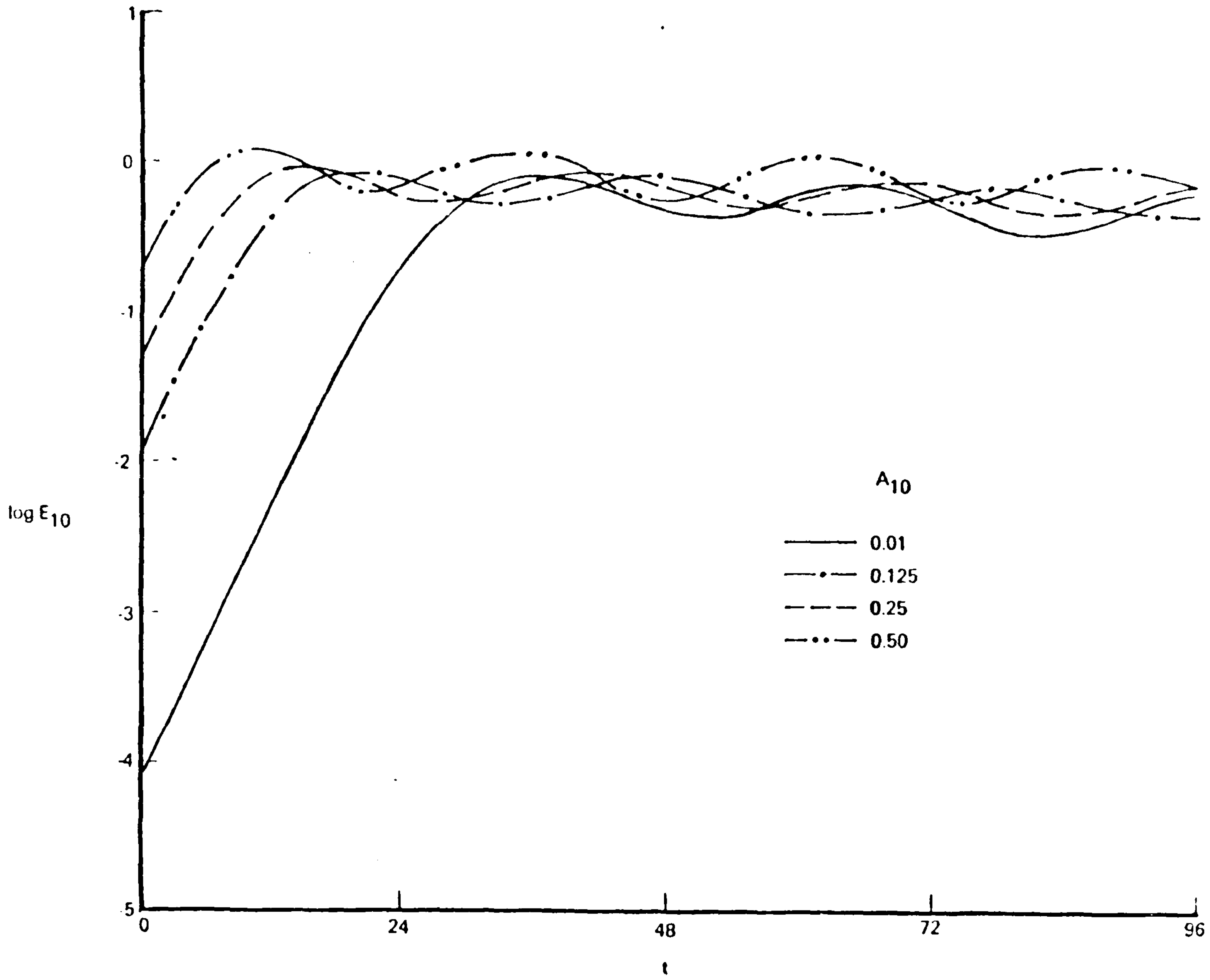
1
0
-1
-2
-3
-4
-5
log E$_{10}$
0
24
48
72
96
t
A$_{10}$
0.01
0.125
0.25
0.50

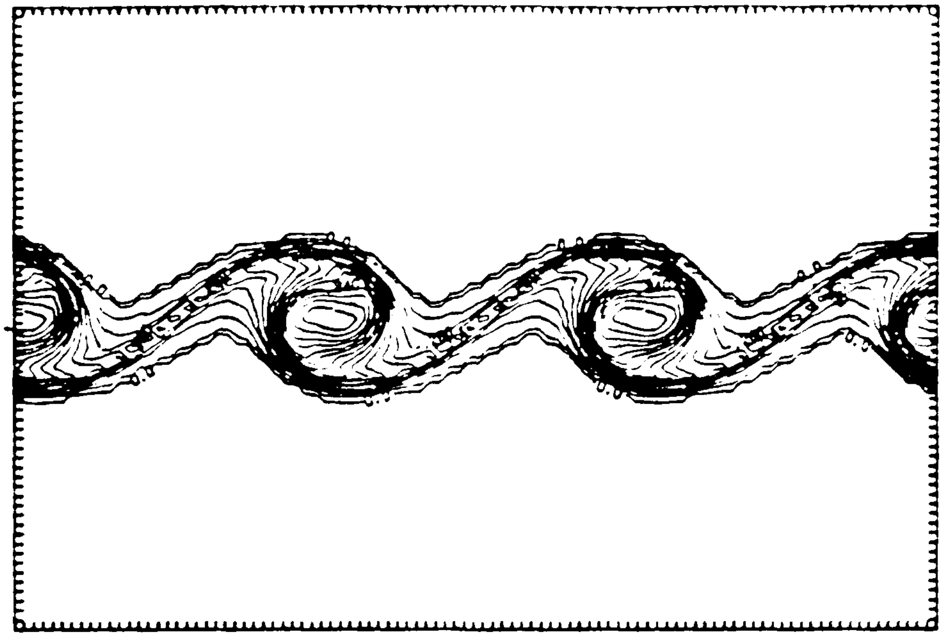

PEAK CONTOUR VALUE IS -1.12. CONTOUR INTERVAL IS 0.07. t = 8.

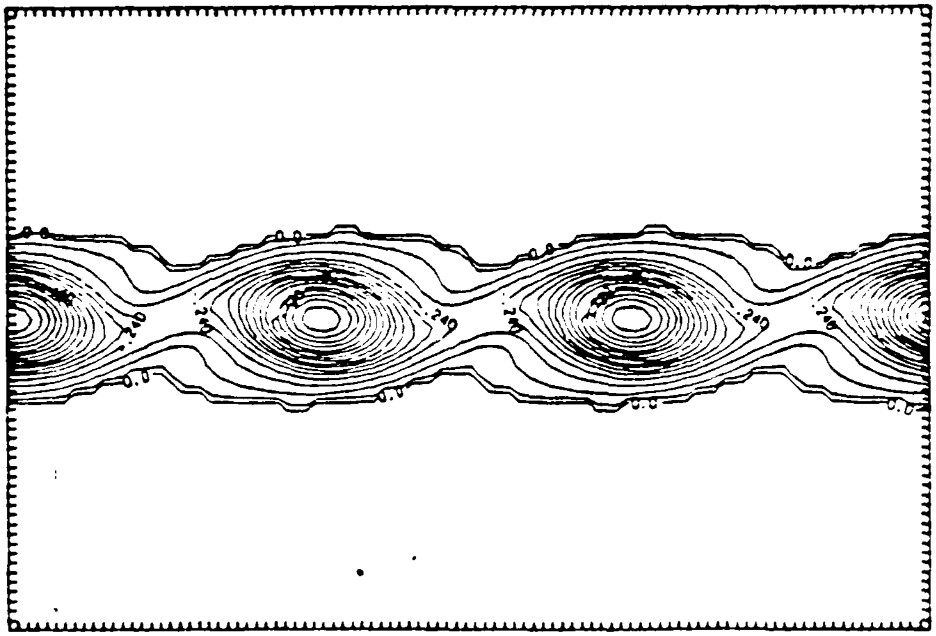

PEAK CONTOUR VALUE IS -0.96. CONTOUR INTERVAL IS 0.07. t = 32.

Fig 2a,b

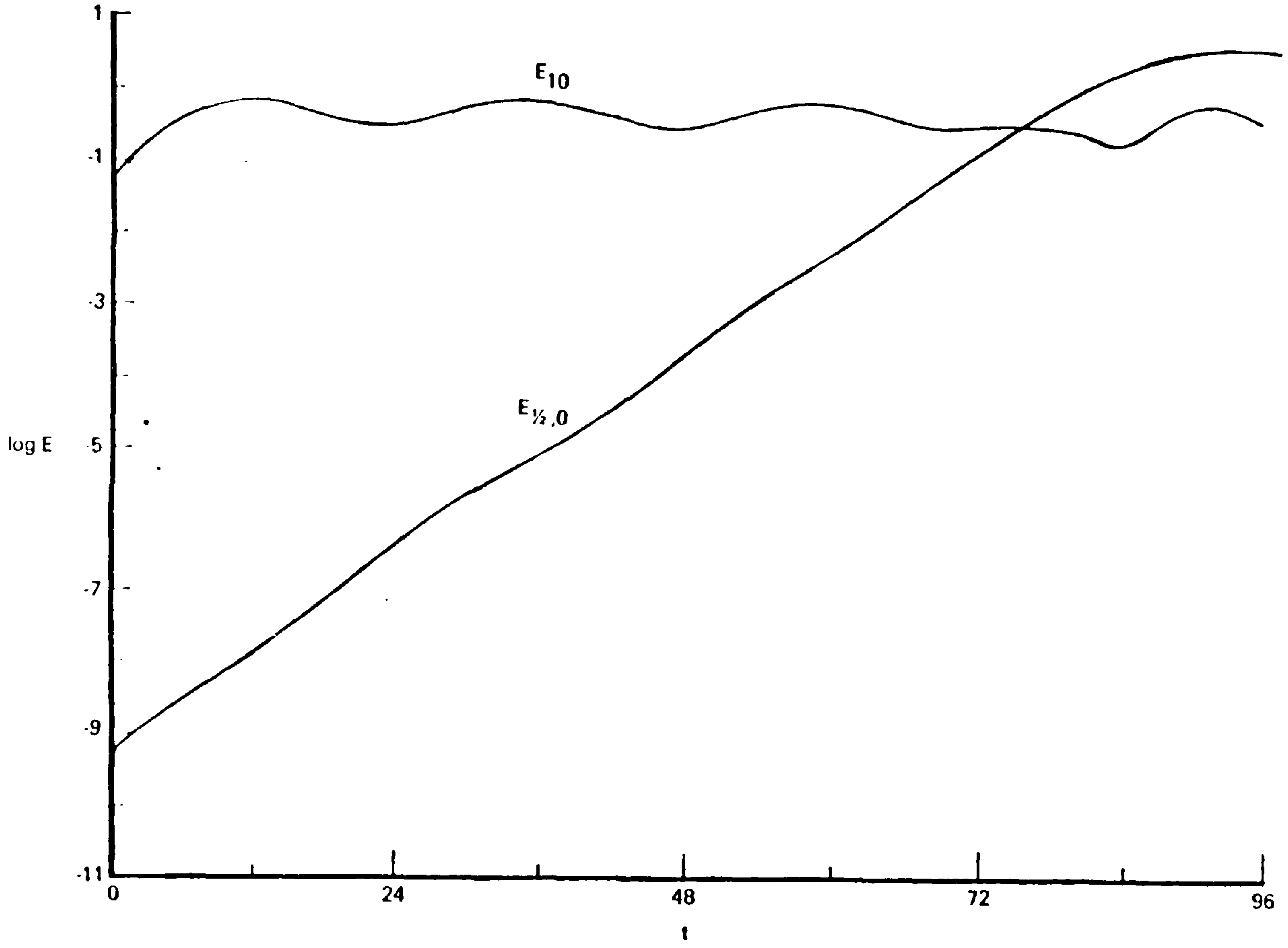

Fig. 3

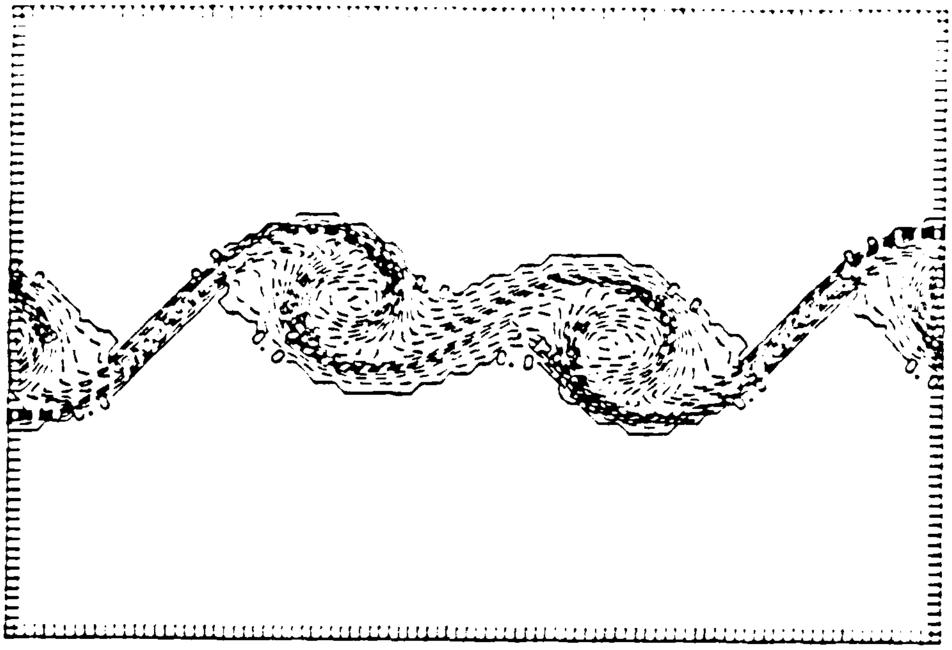

PEAK CONTOUR VALUE IS -1.28. CONTOUR INTERVAL IS 0.08. t = 8.

Fig. 4a,b

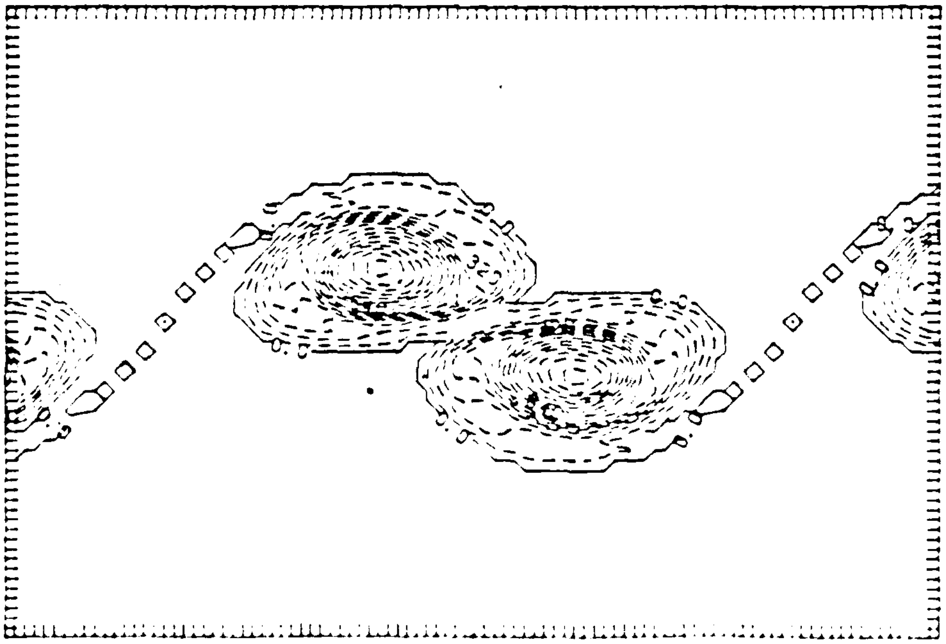

PEAK CONTOUR VALUE IS -1.20. CONTOUR INTERVAL IS 0.08. t = 16.

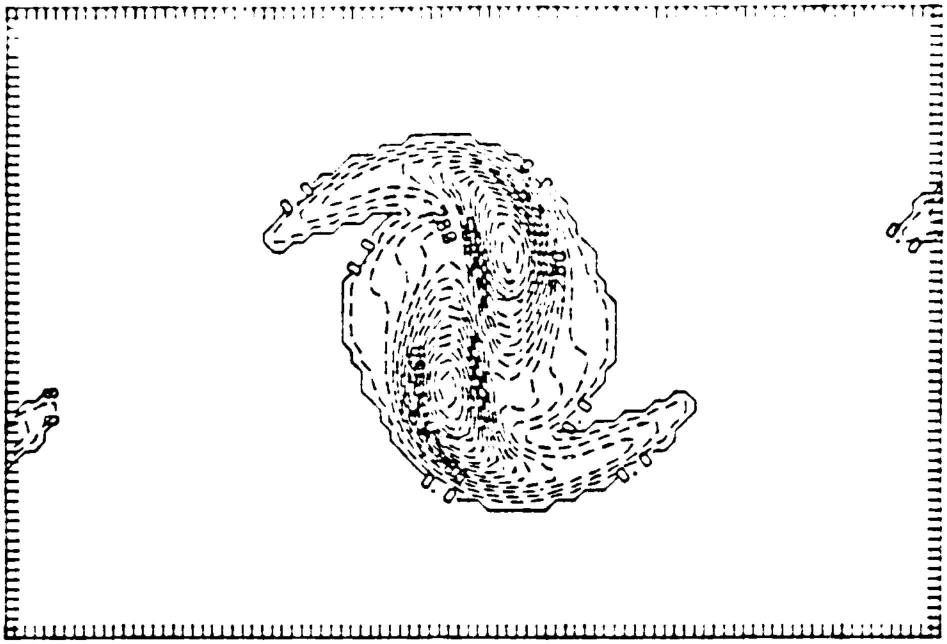

PEAK CONTOUR VALUE IS -1.12. CONTOUR INTERVAL IS 0.07. t = 24.

Fig. 4c, d

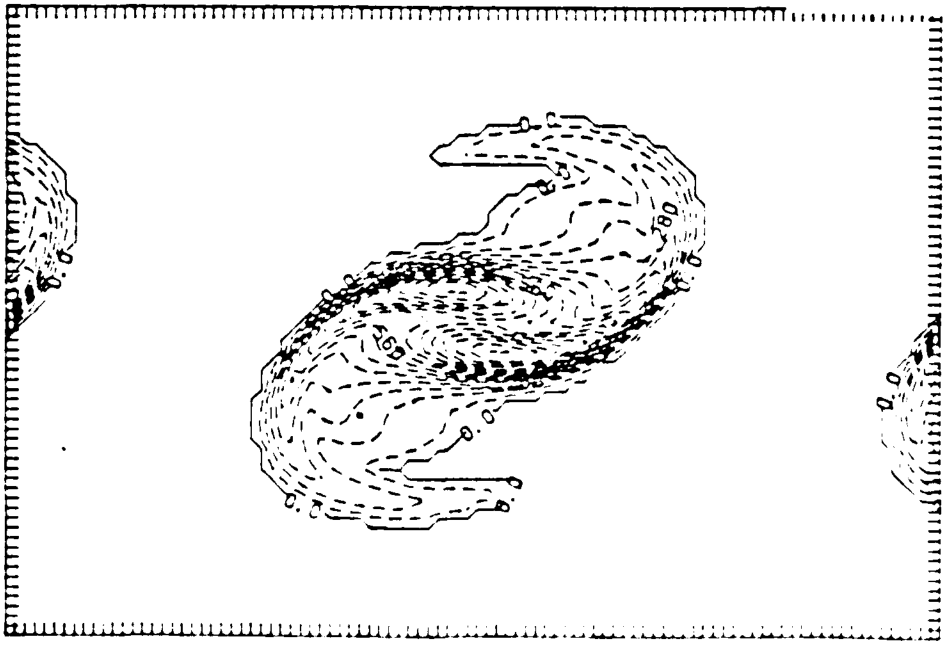

PEAK CONTOUR VALUE IS -1.05. CONTOUR INTERVAL IS 0.07. t = 32.

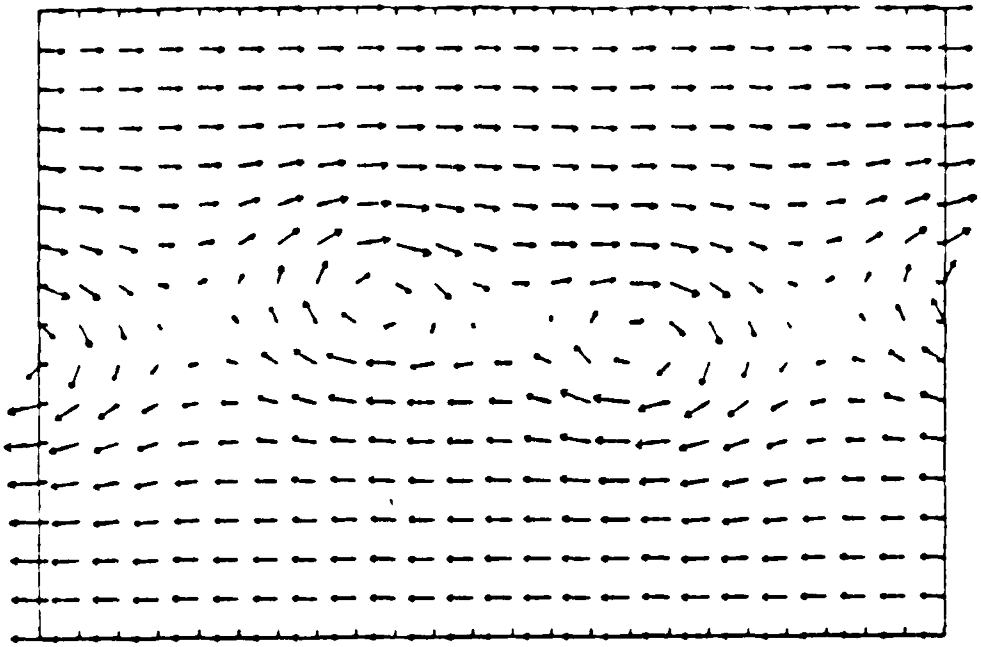

PEAK VELOCITY IS 0.702. t = 8

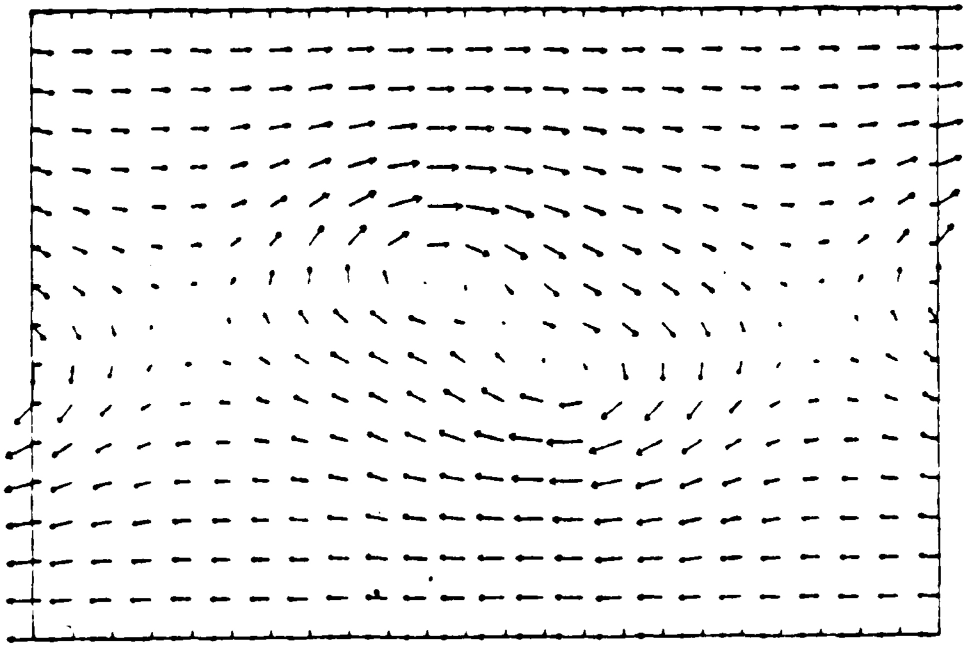

PEAK VELOCITY IS 0.783. t = 16.

Fig 5a, b

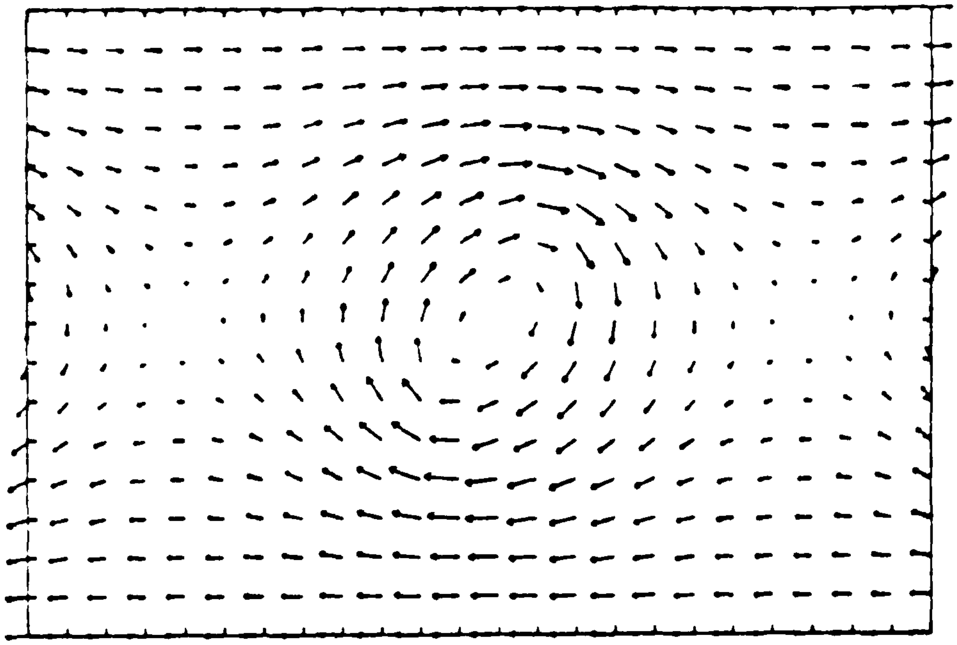

PEAK VELOCITY IS 0.800. t = 24.

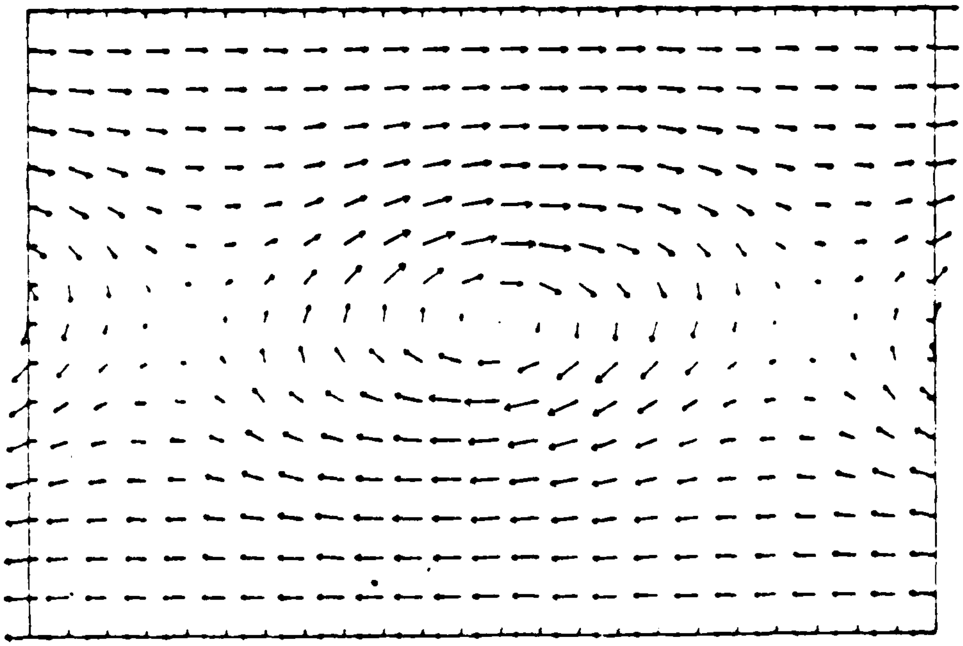

PEAK VELOCITY IS 0.714. t = 32.

Fig 5c,d

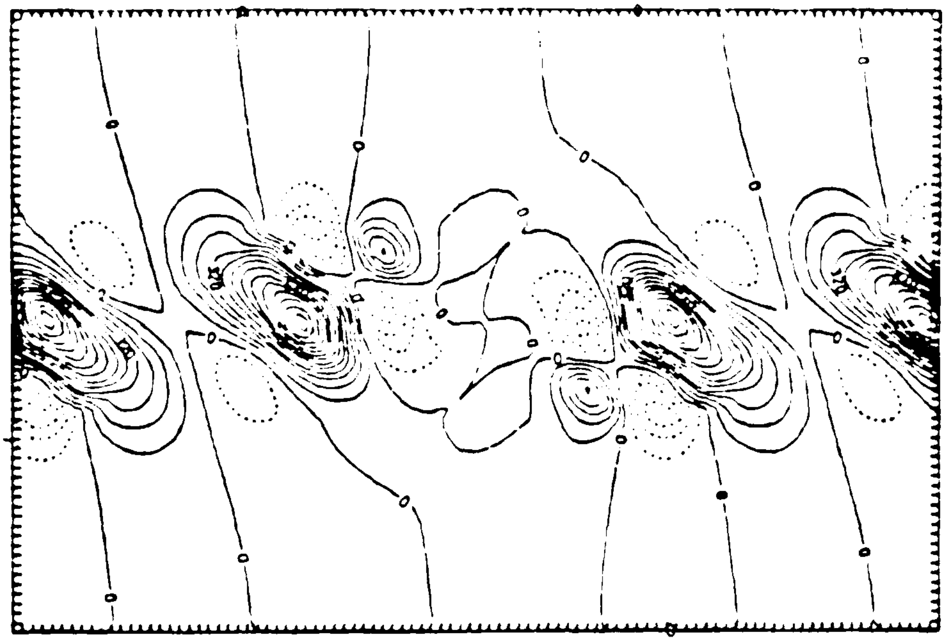

CONTOURS ARE FROM −0.032 to 0.104. CONTOUR INTERVAL IS 0.008. $t = 8$.

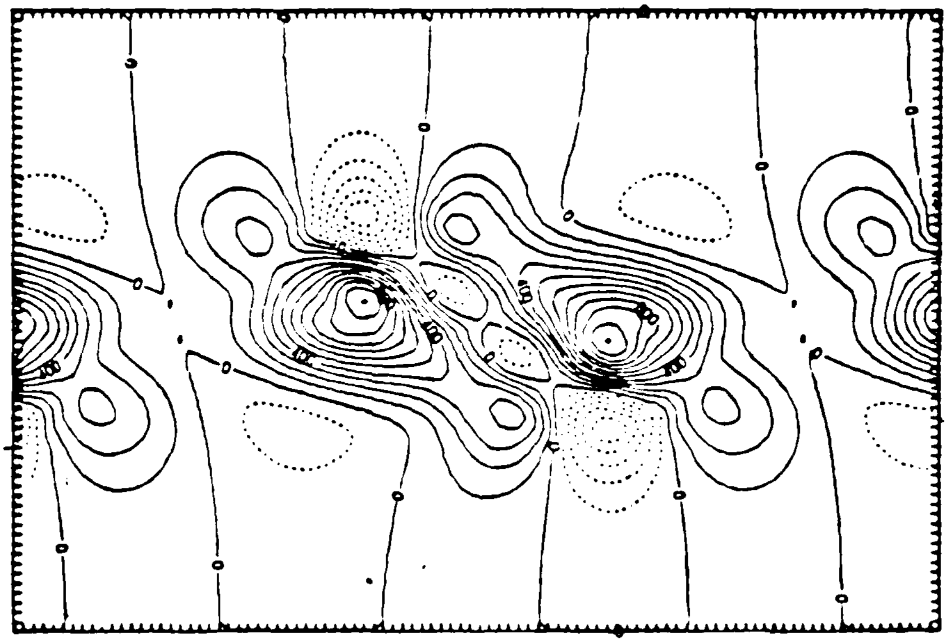

CONTOURS ARE FROM -0.05 TO 0.11. CONTOUR INTERVAL IS 0.01. $t = 16$.

Fig 6a 2

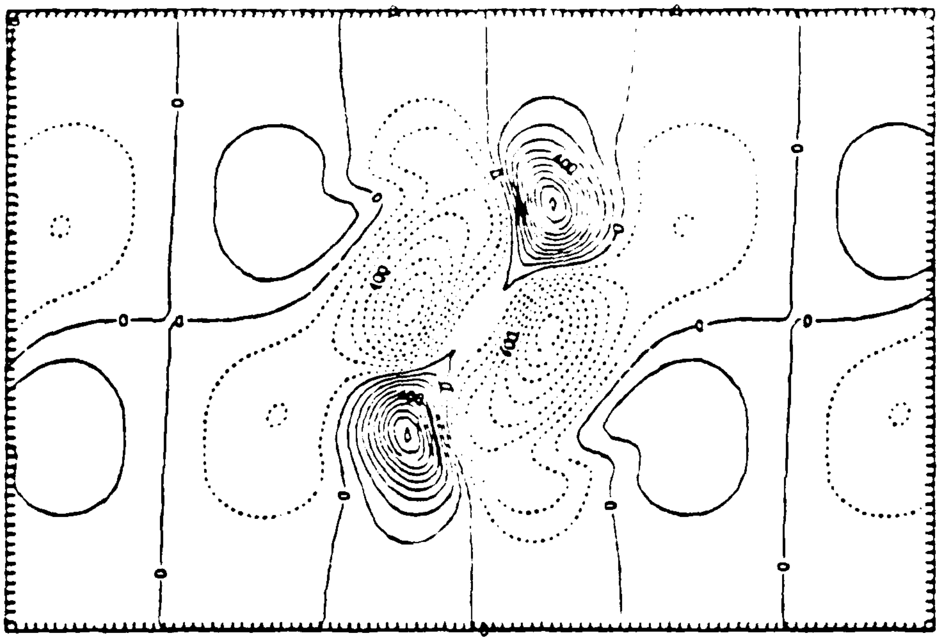

CONTOURS ARE FROM -0.08 TO 0.1. CONTOUR INTERVAL IS 0.01. t = 24.

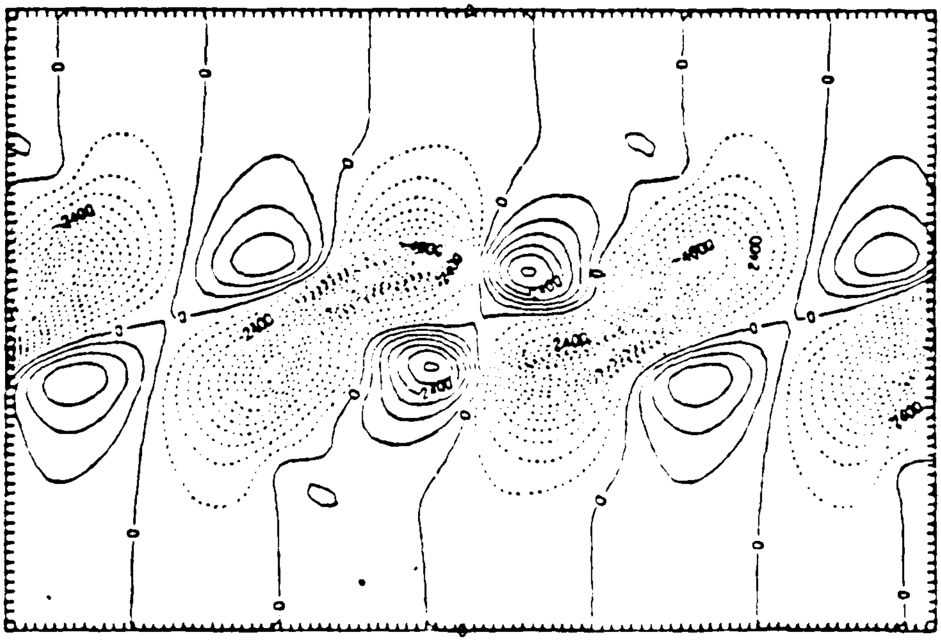

CONTOURS ARE FROM -0.072 TO 0.036. CONTOUR INTERVAL IS 0.006. t = 32.

Fig 6c,d

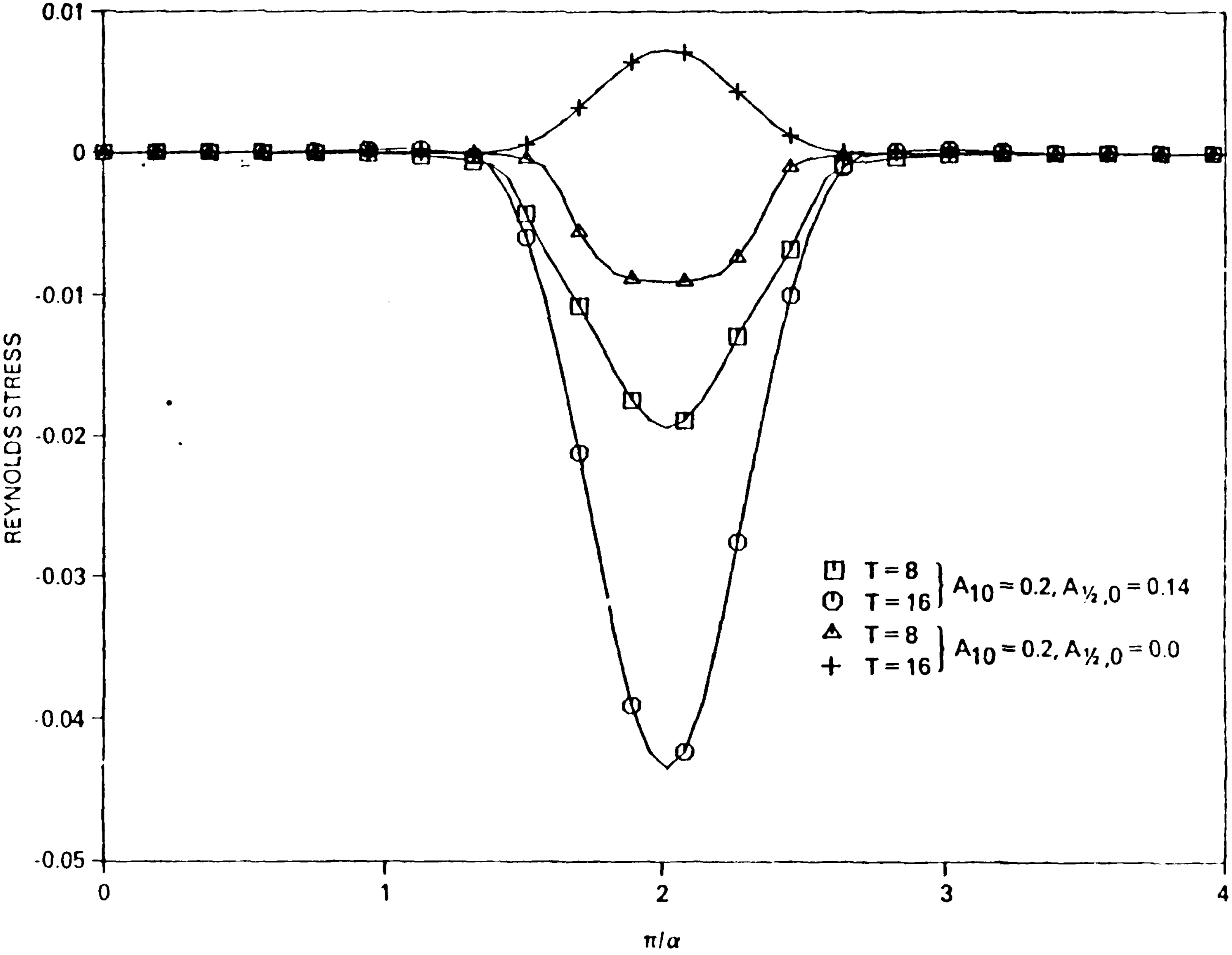
0.01
0
-0.01
-0.02
-0.03
-0.04
-0.05
REYNOLDS STRESS
0
1
2
3
4
π/α
□ T = 8
○ T = 16
} $A_{10} = 0.2, A_{1/2,0} = 0.14$
△ T = 8
+ T = 16
} $A_{10} = 0.2, A_{1/2,0} = 0.0$

Fig 6e

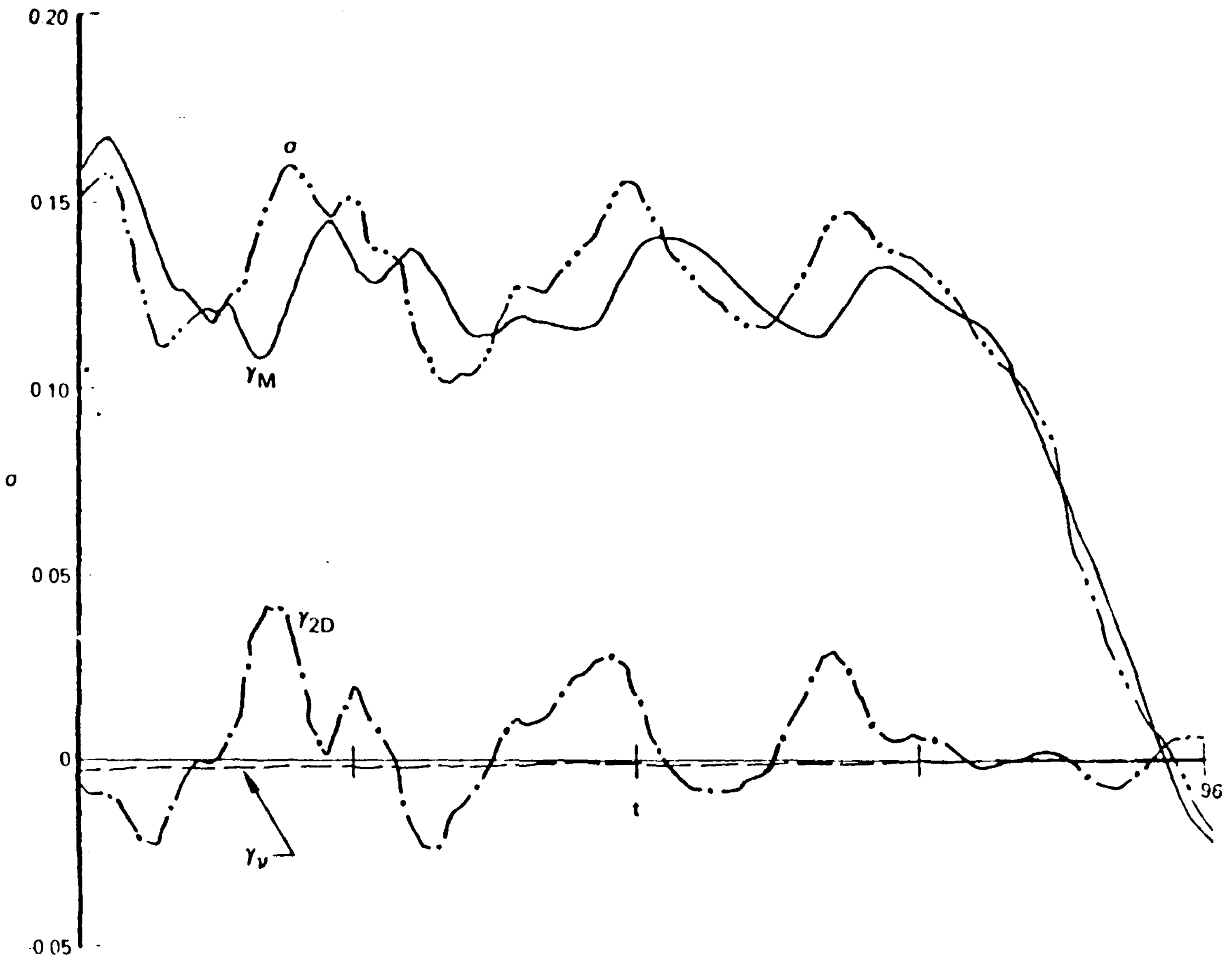

Fig 7

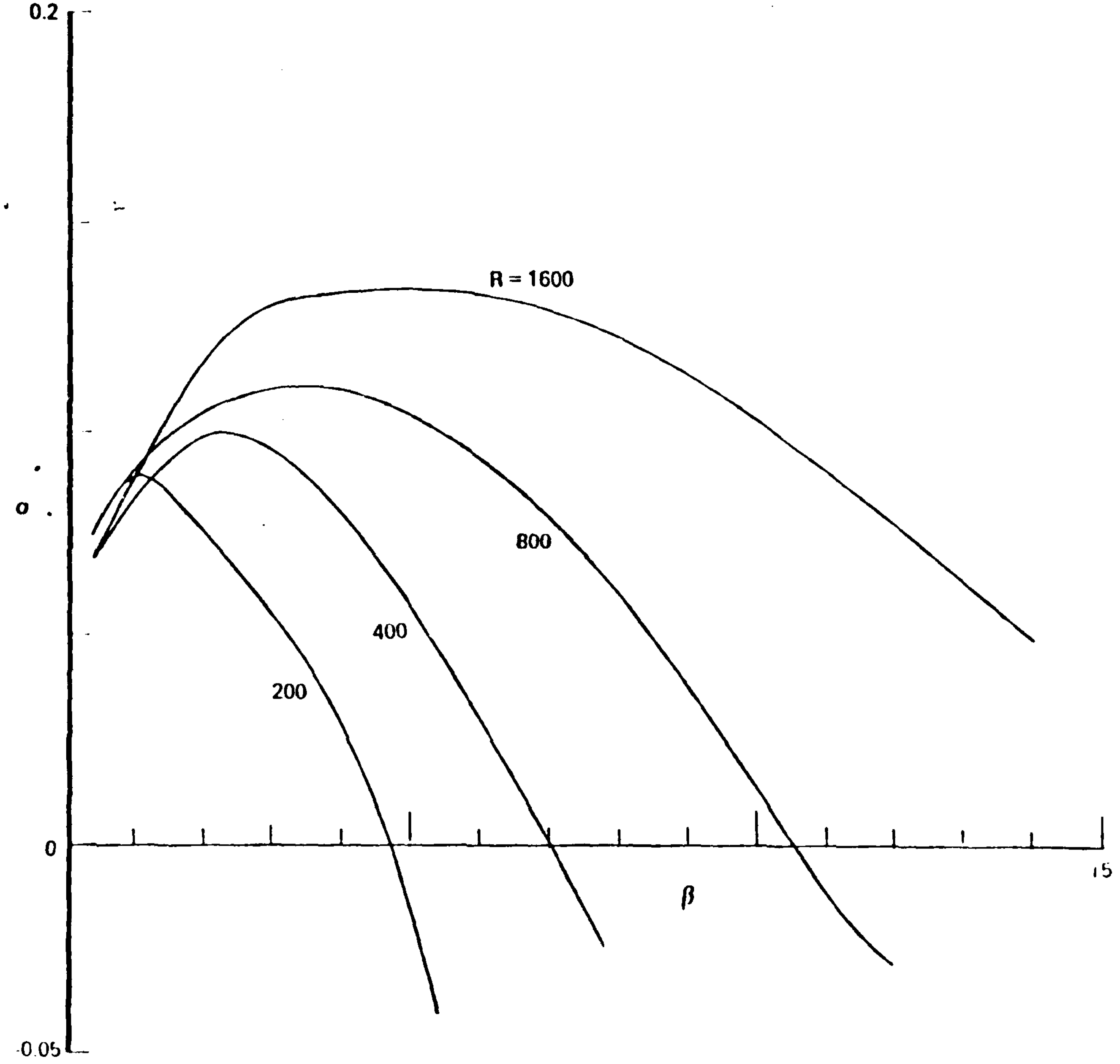

Fig. 8

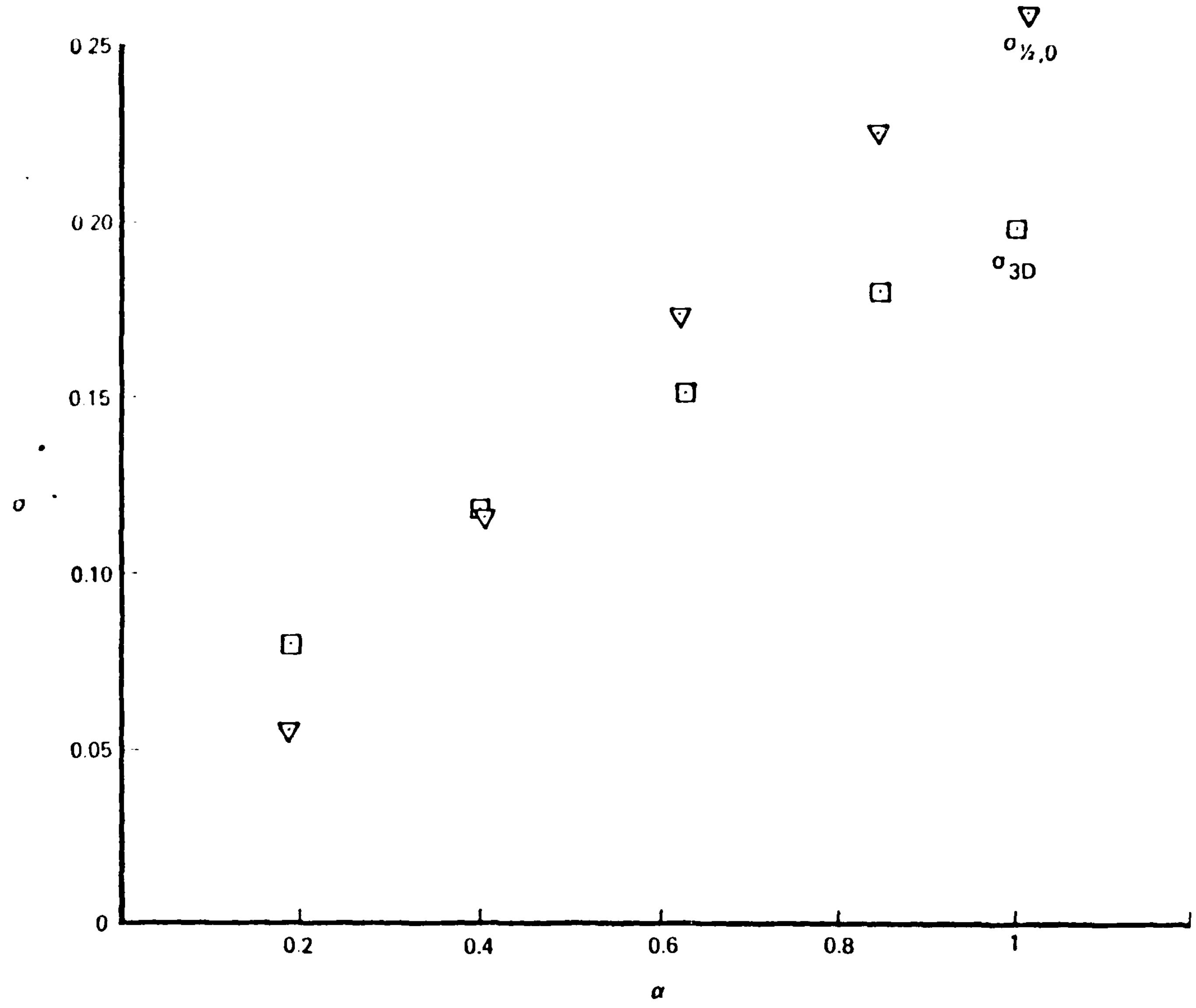

Fig. 9

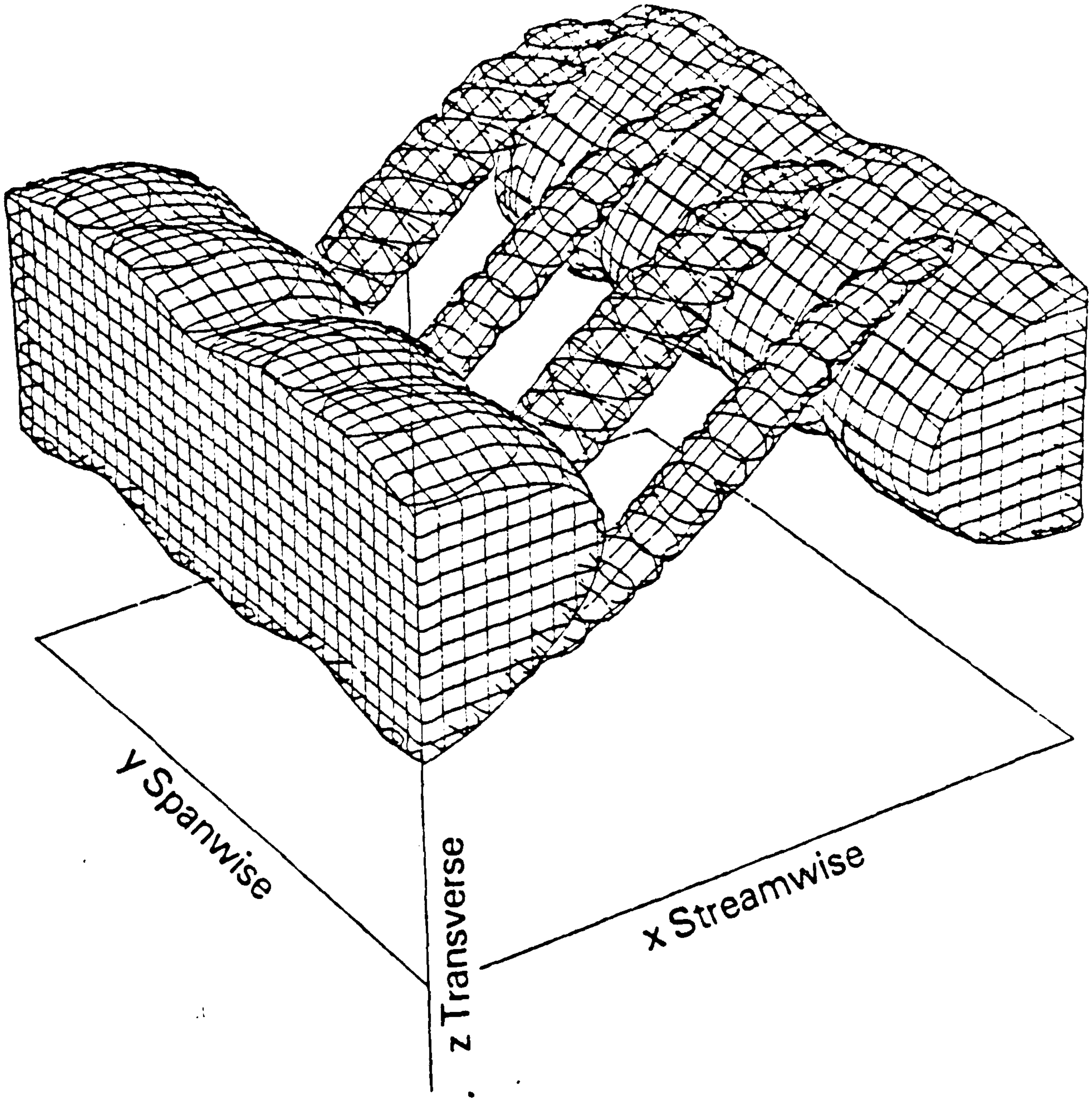
y Spanwise
z Transverse
x Streamwise

$|\omega_x| + |\omega_y| + |\omega_z|$

Fig 10

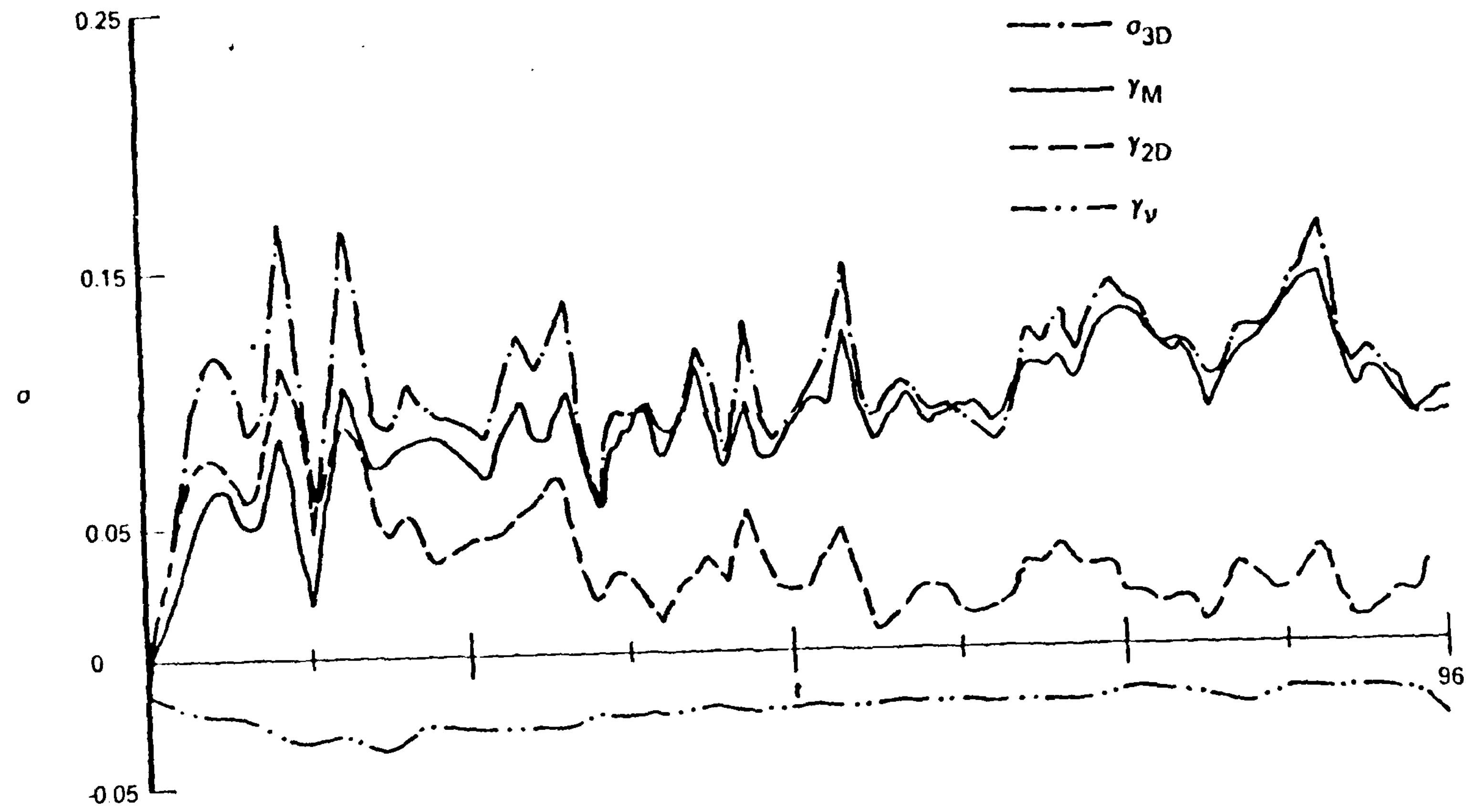

Fig 11a

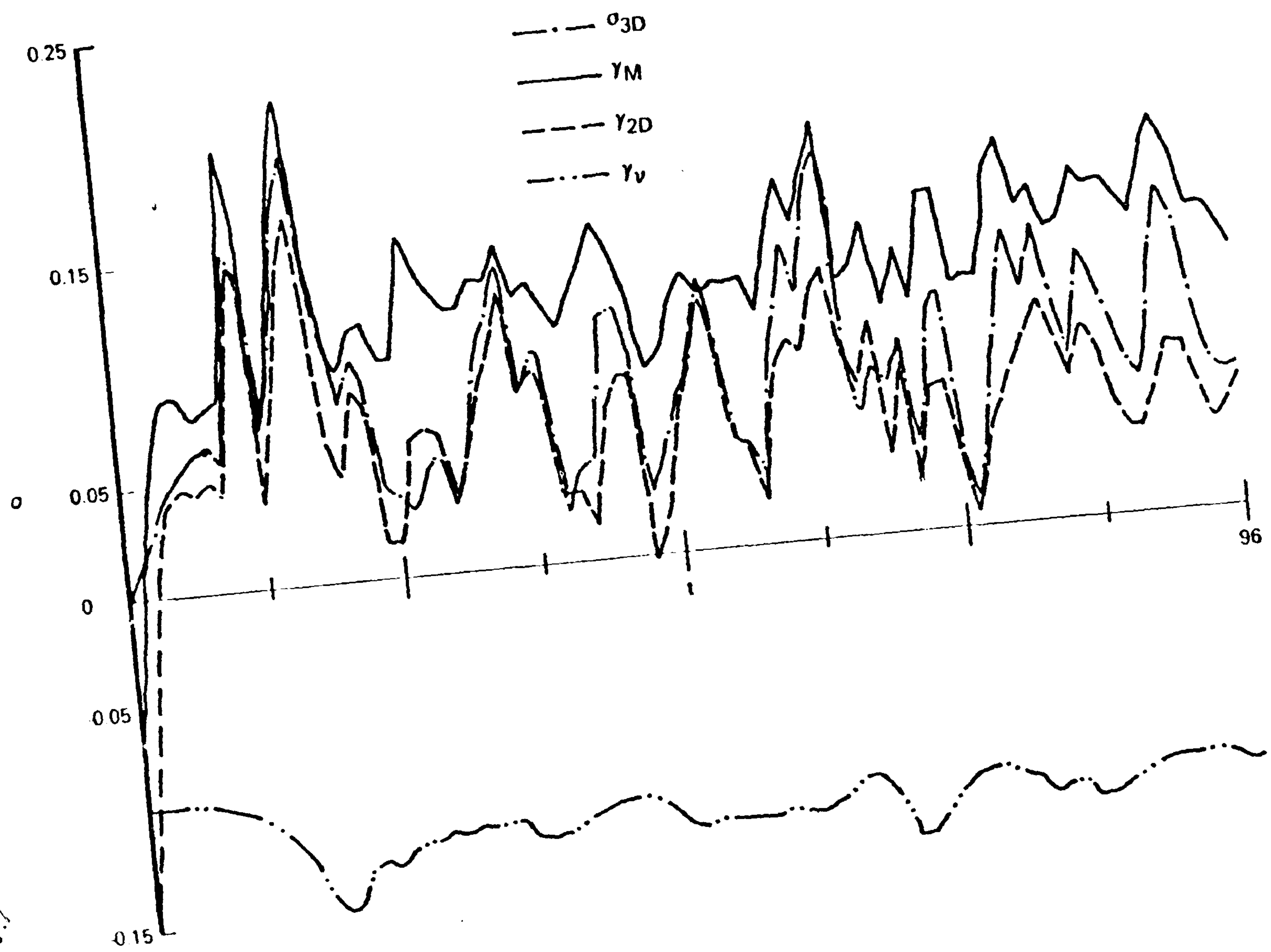

Fig. 11b

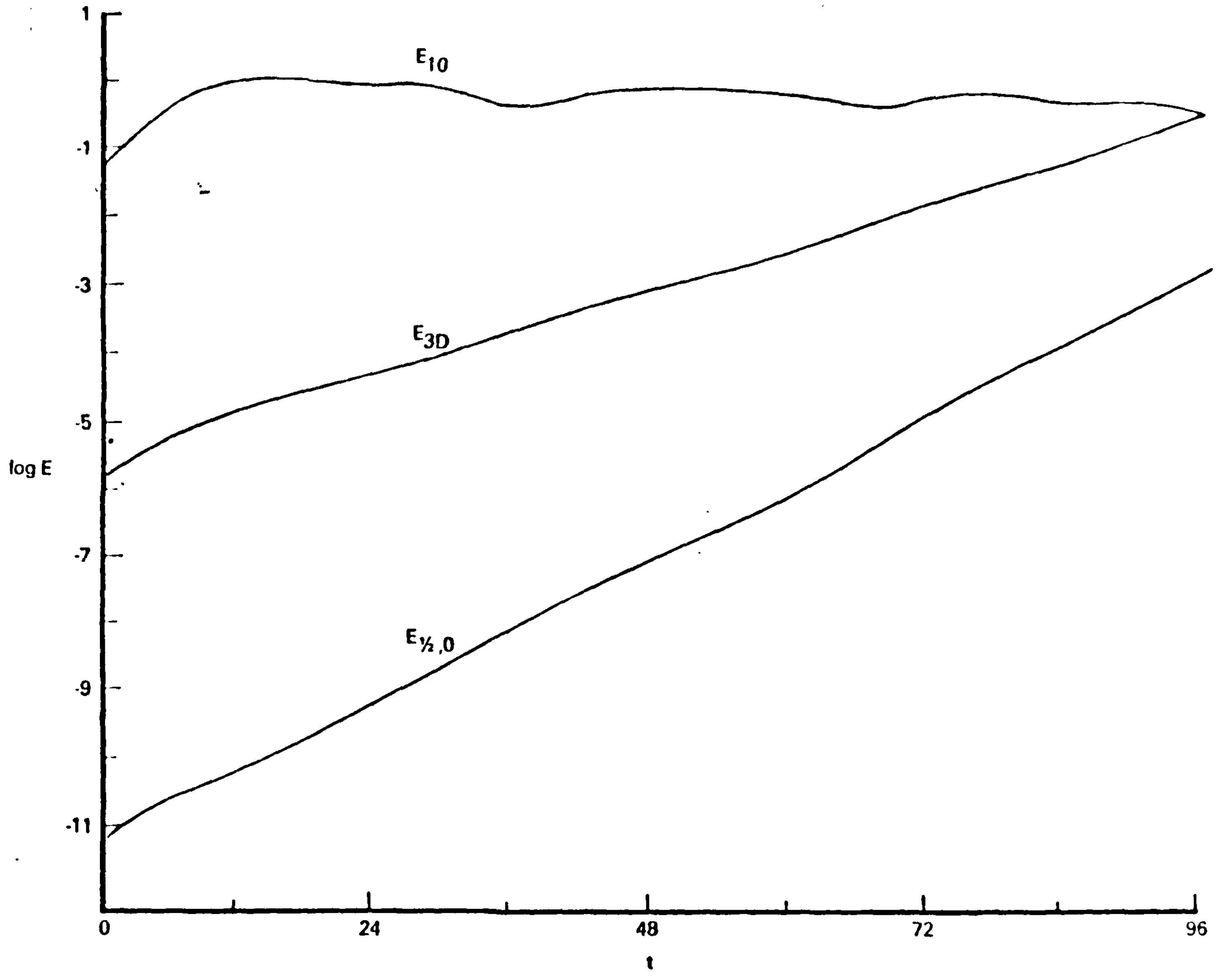

Fig. 12

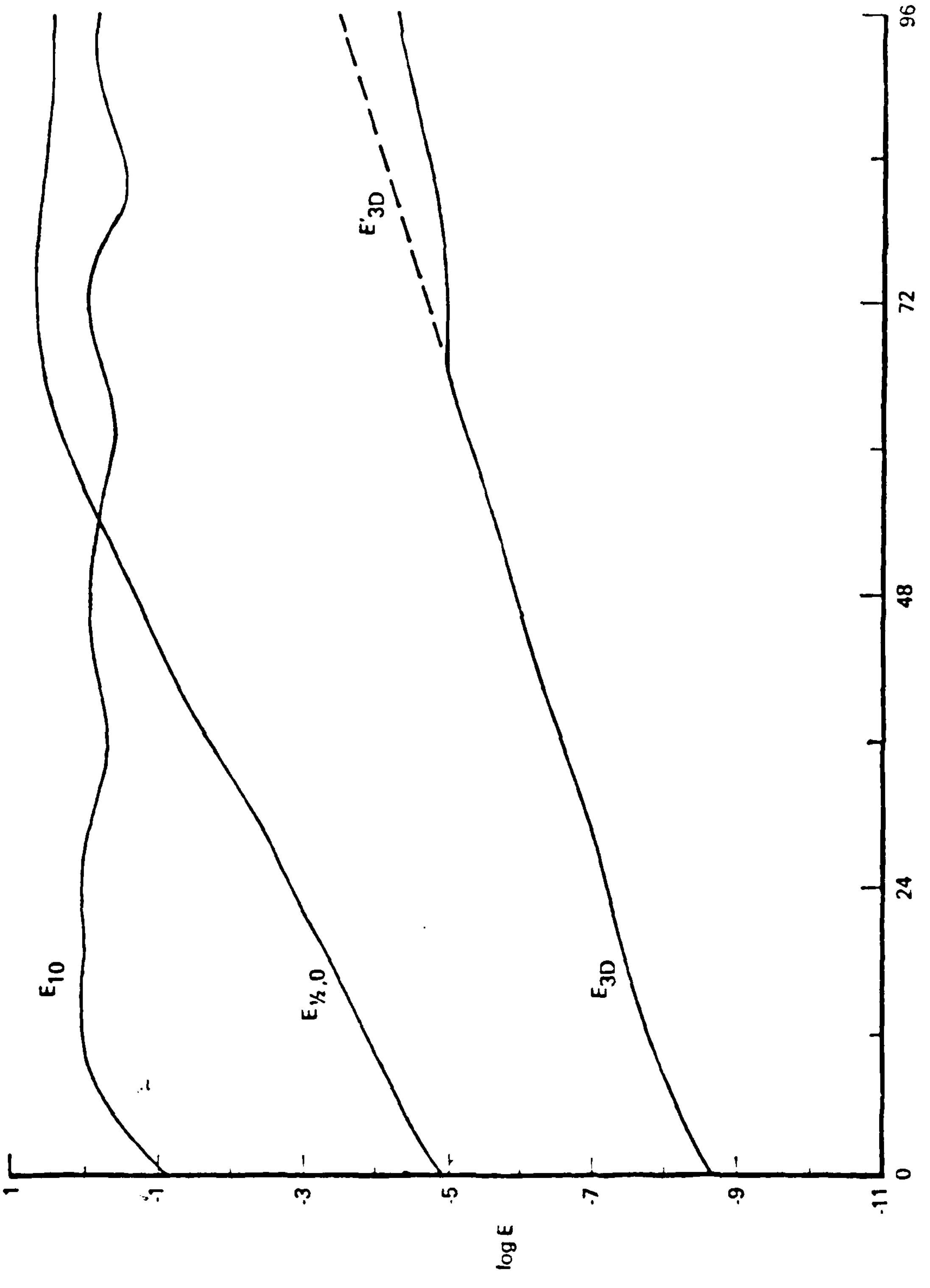

Fig 13

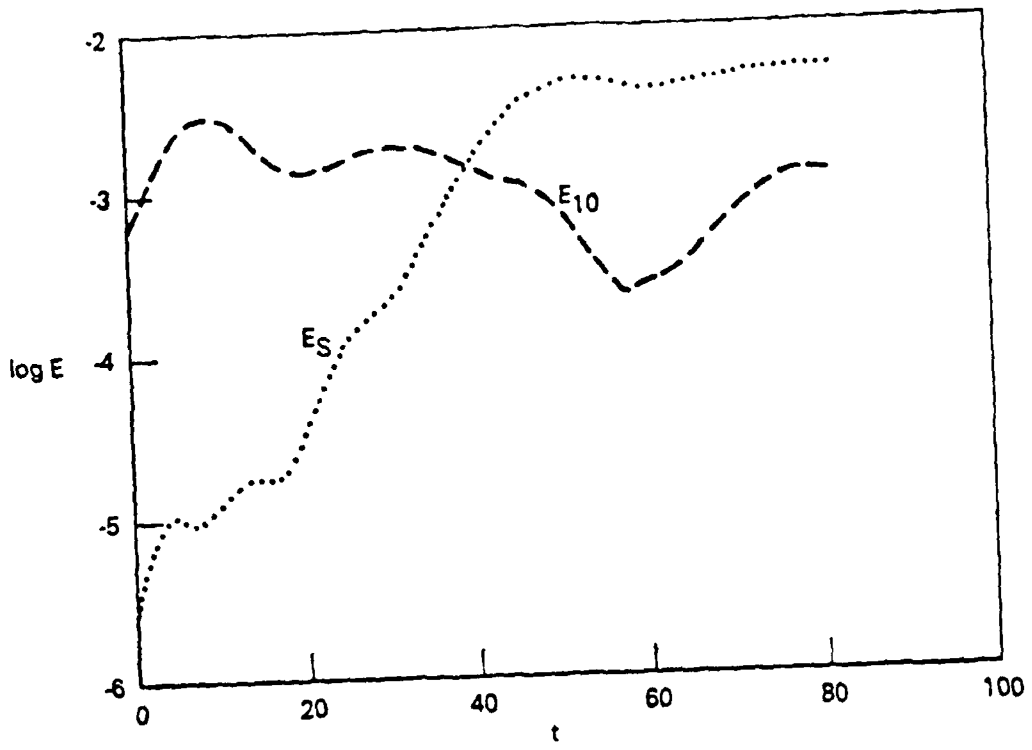

Fig. 14a

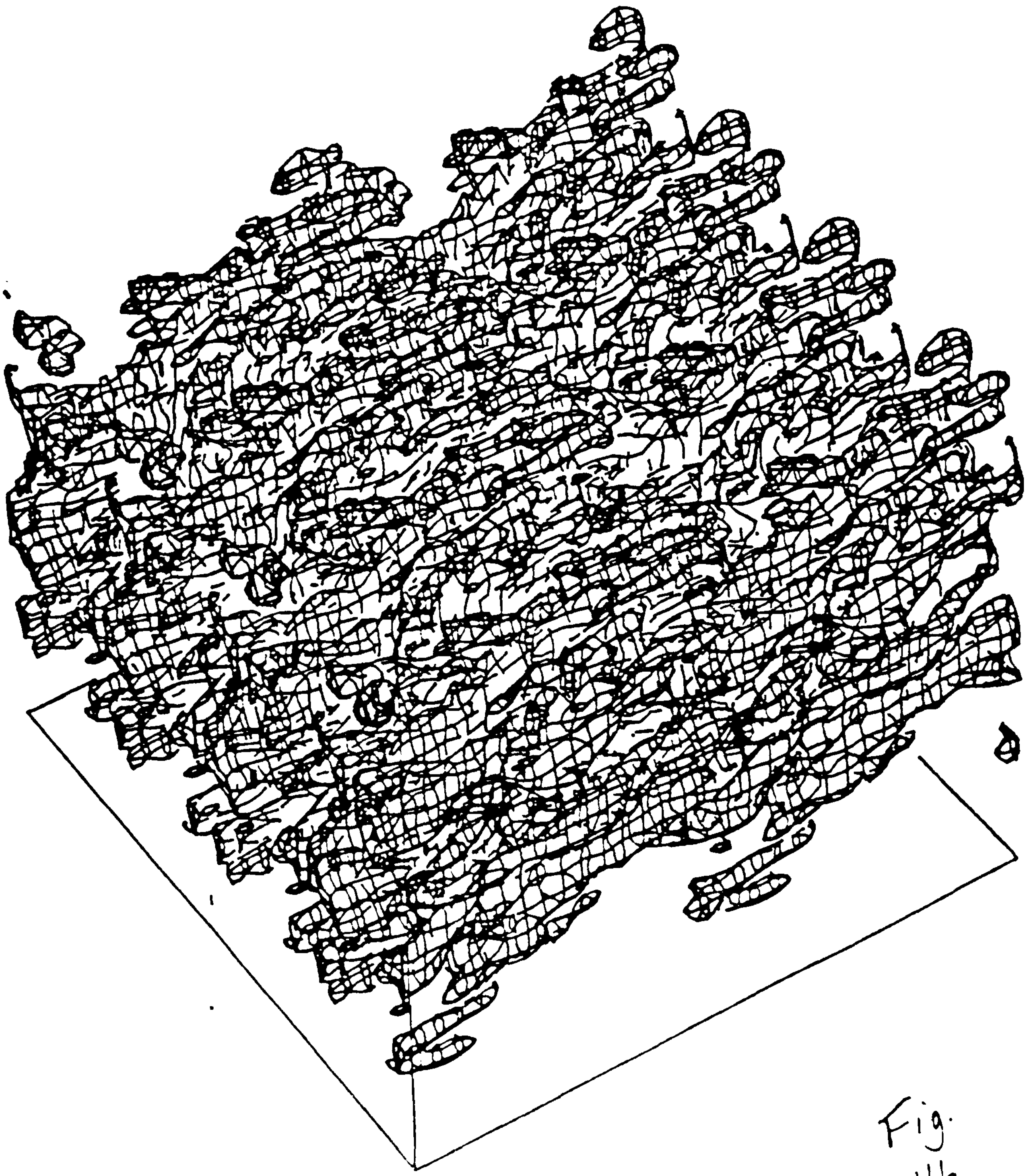

Fig. 14b

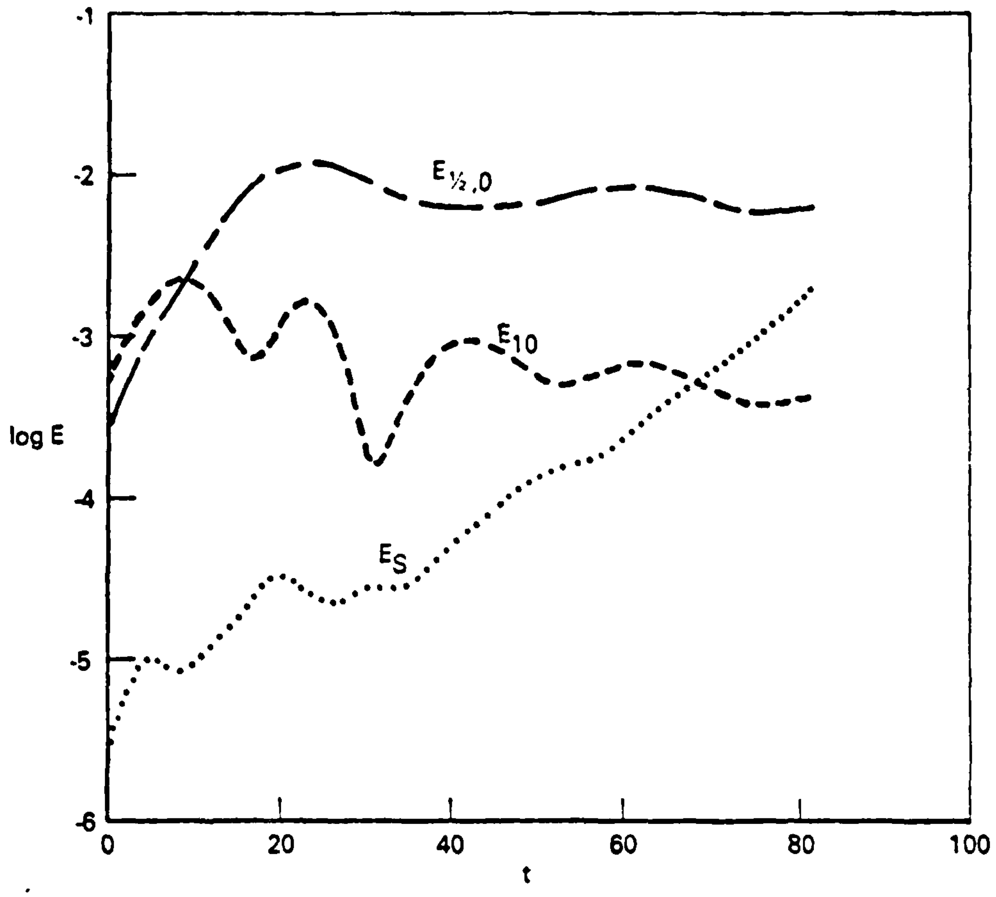

Fig. 14c

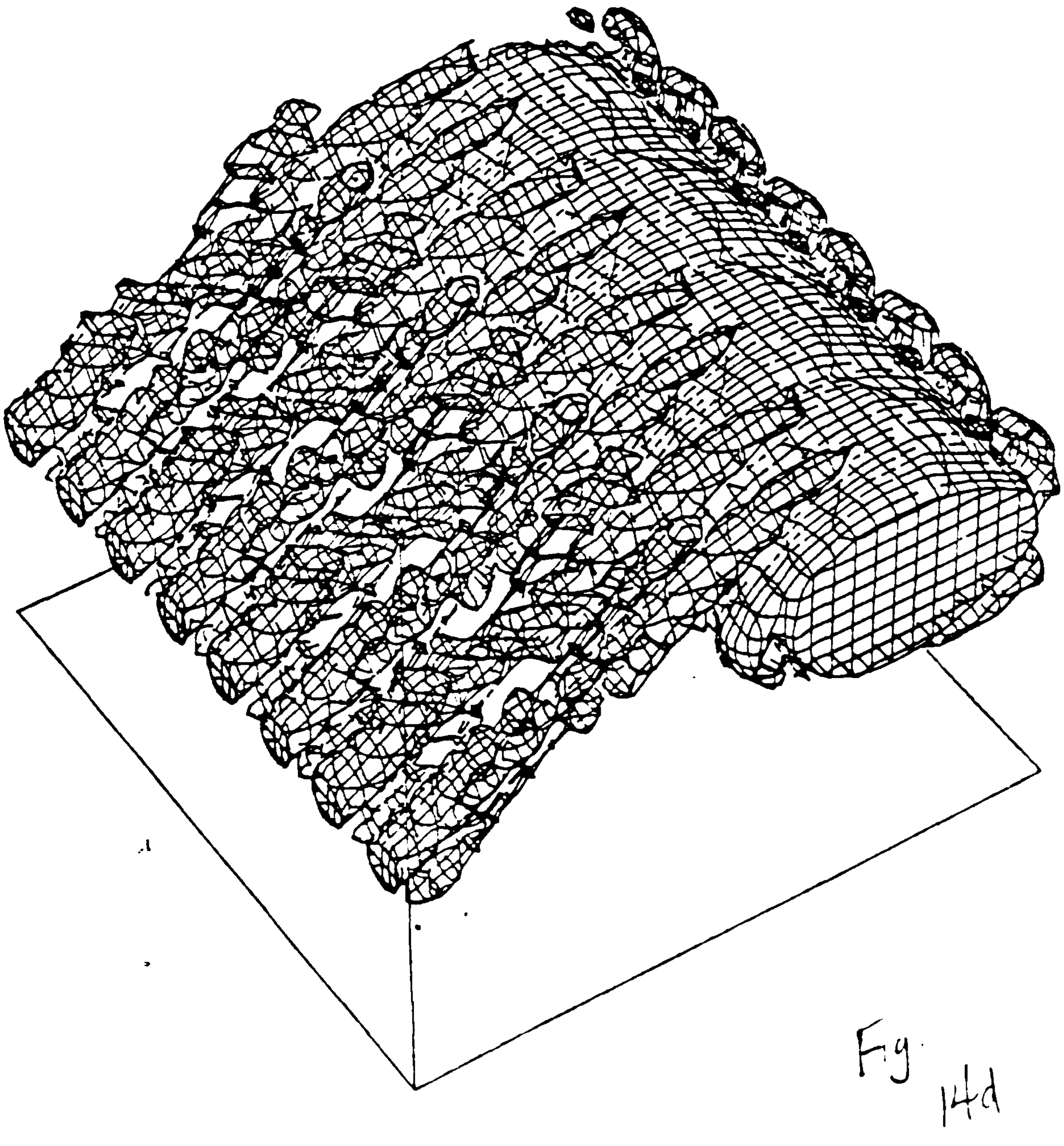

Fig 14d

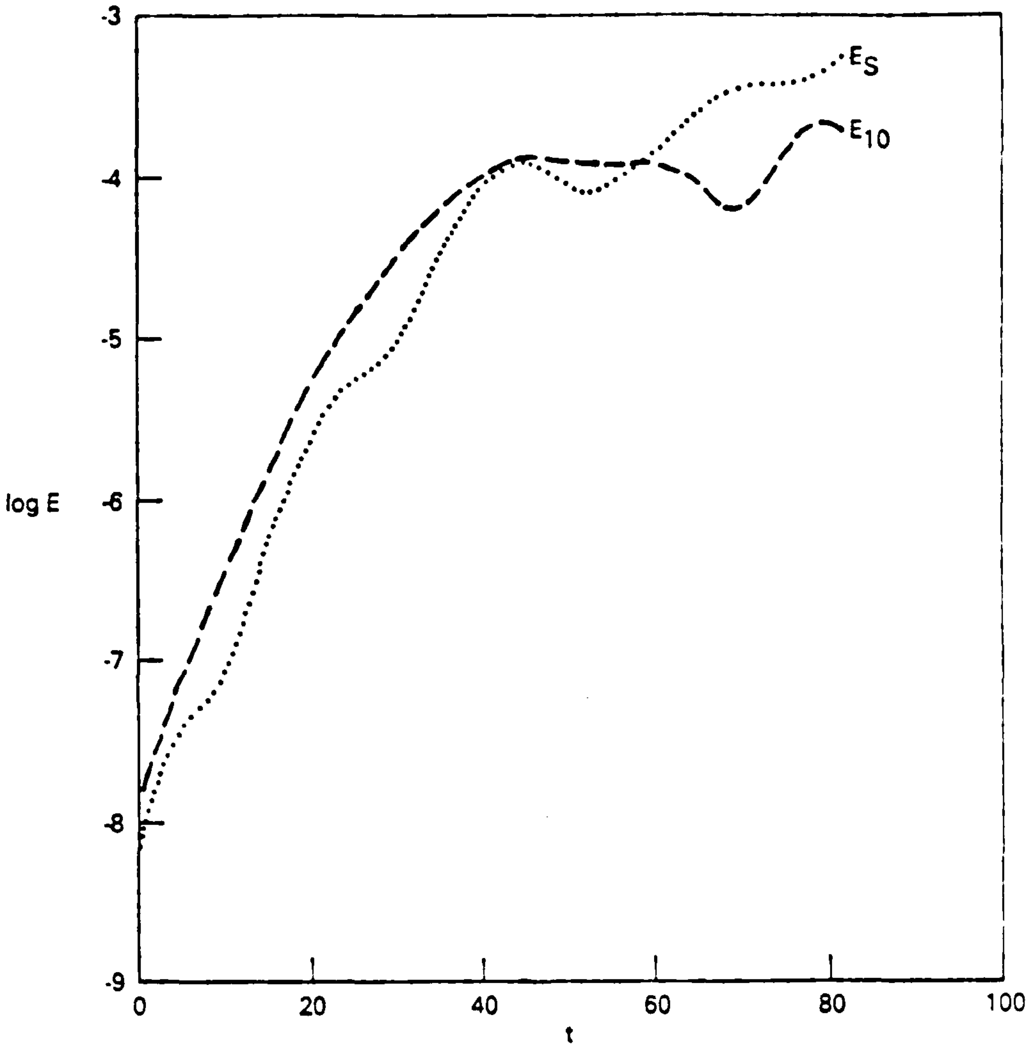

Fig. 15a

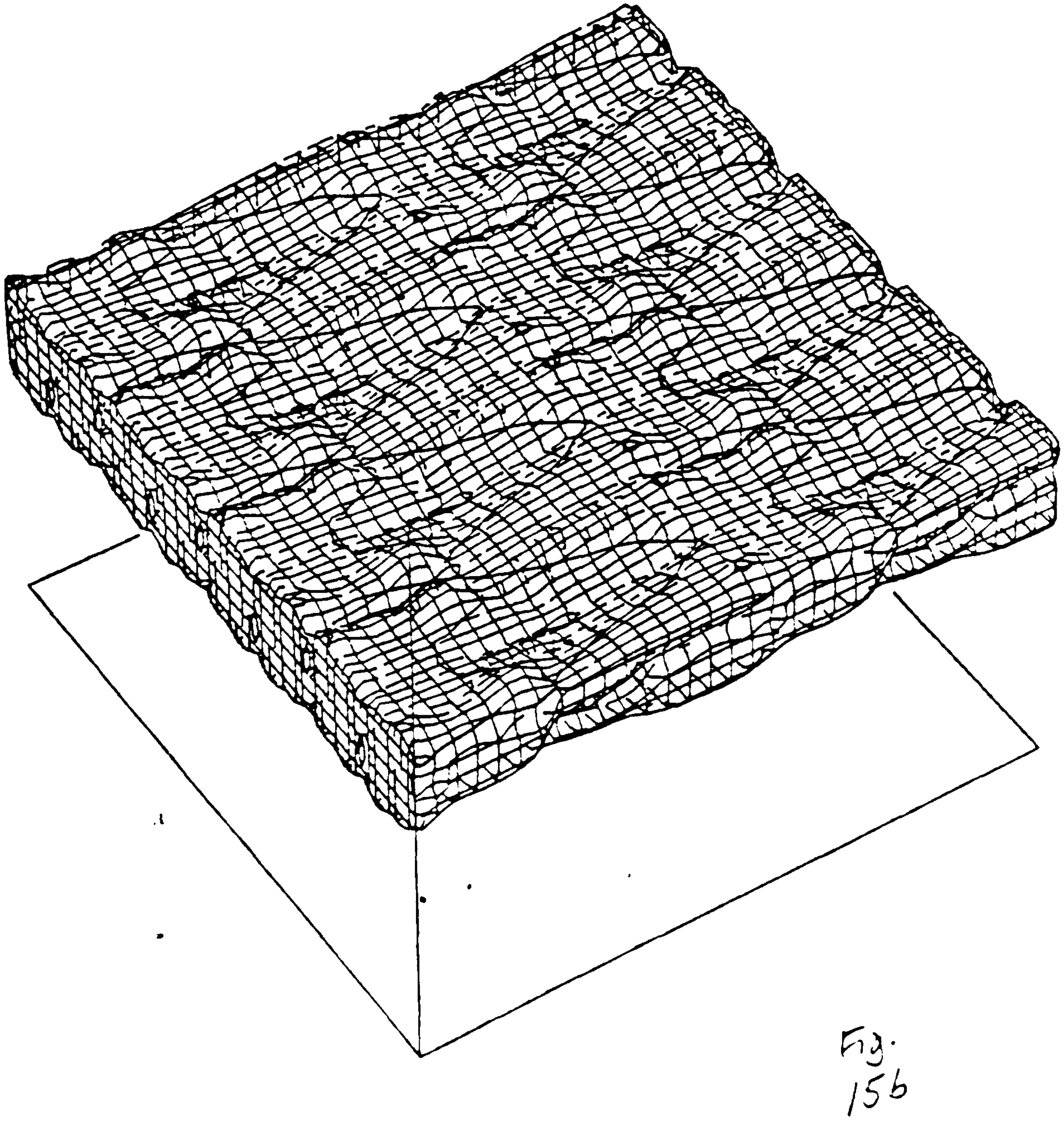

Fig. 15b

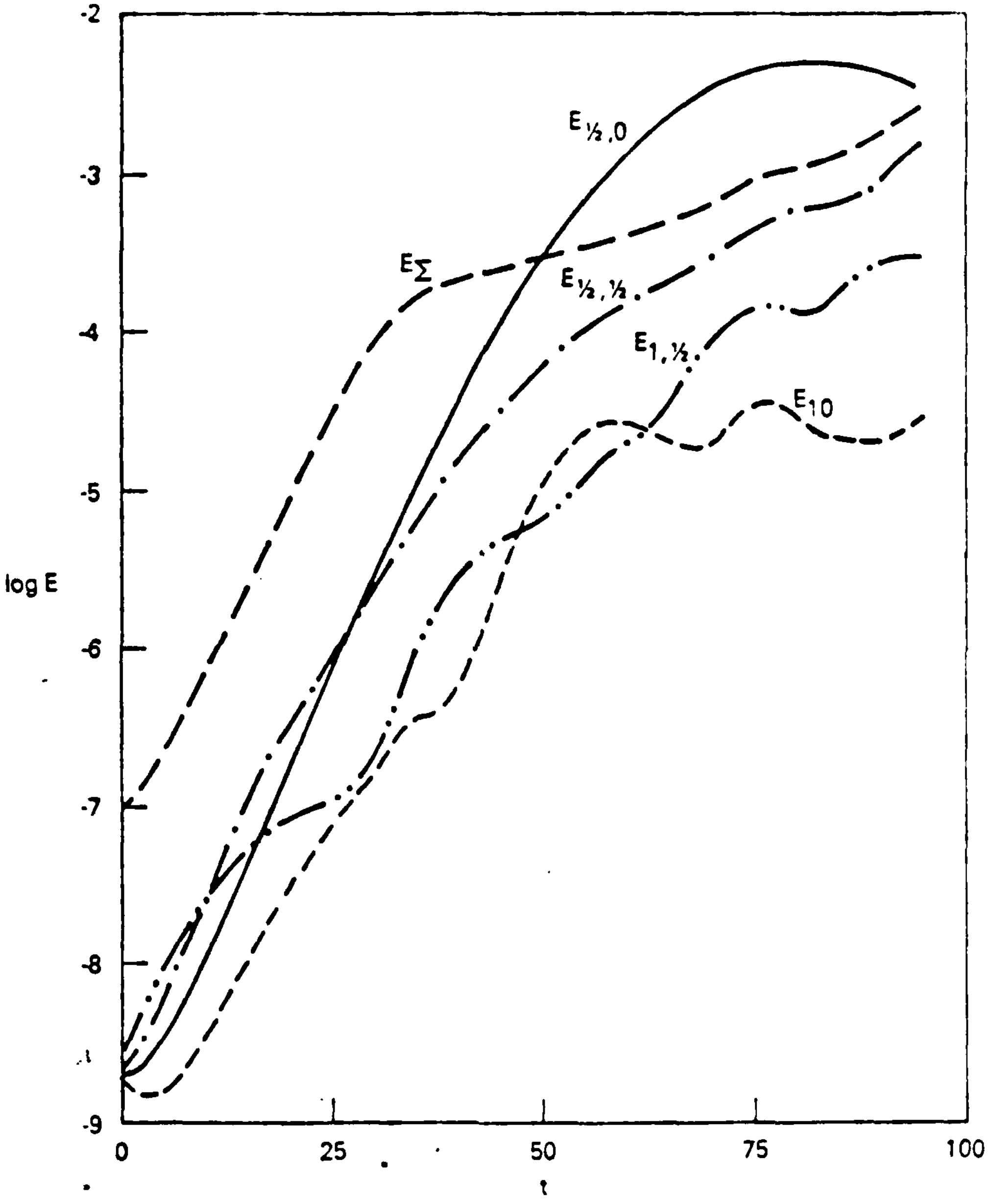

Fig.
16a

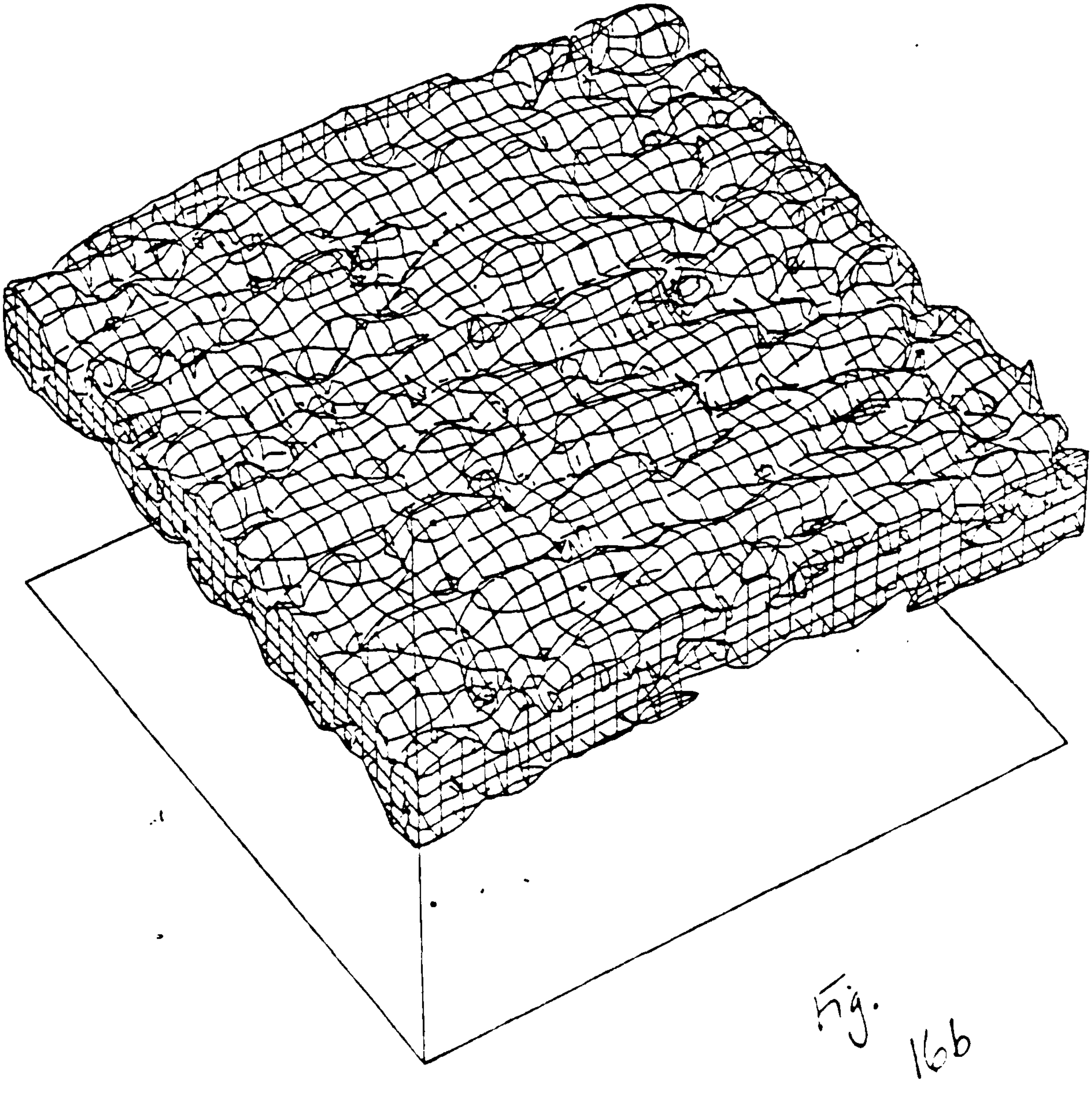

Fig. 16b

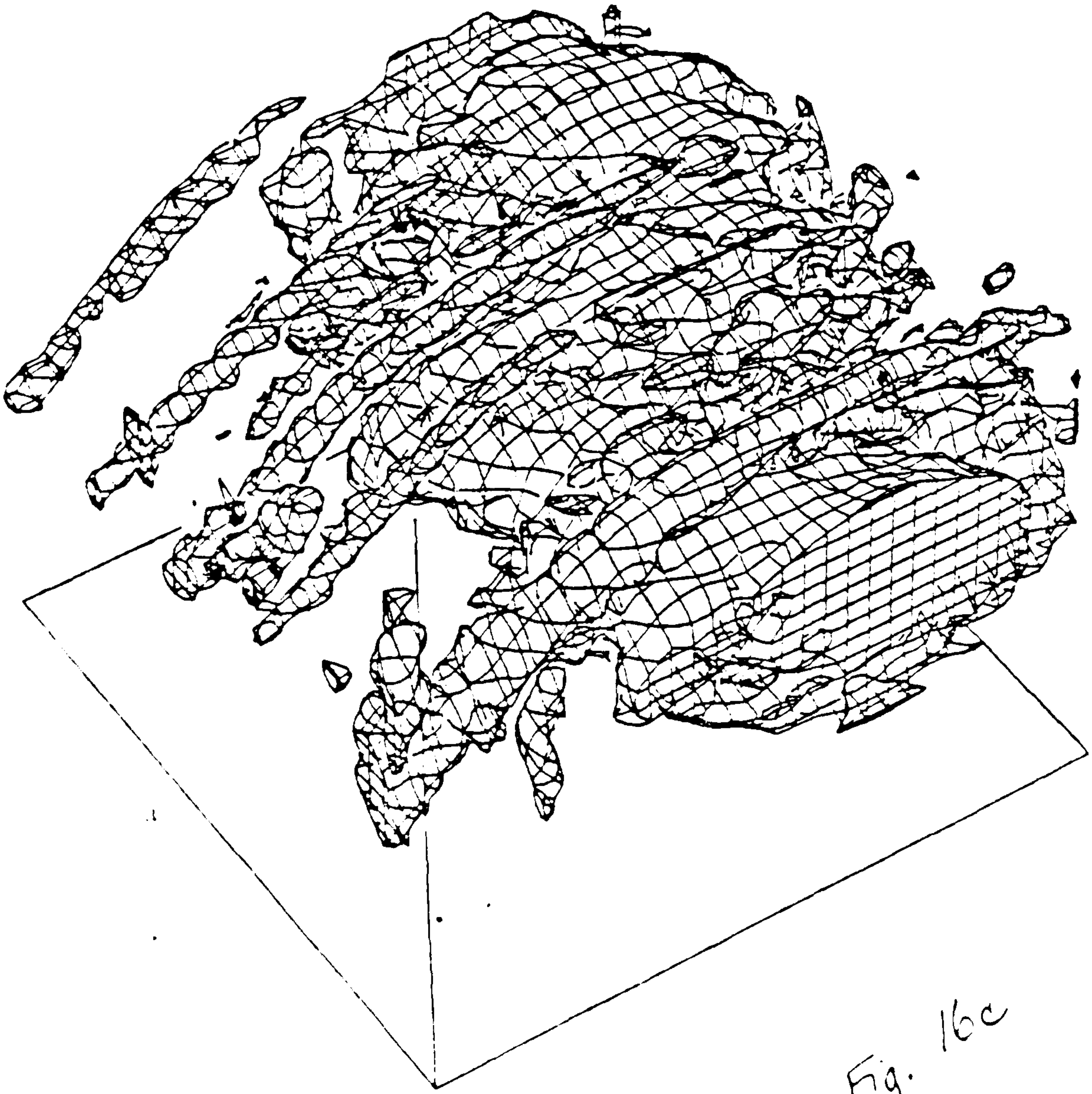

Fig. 16c

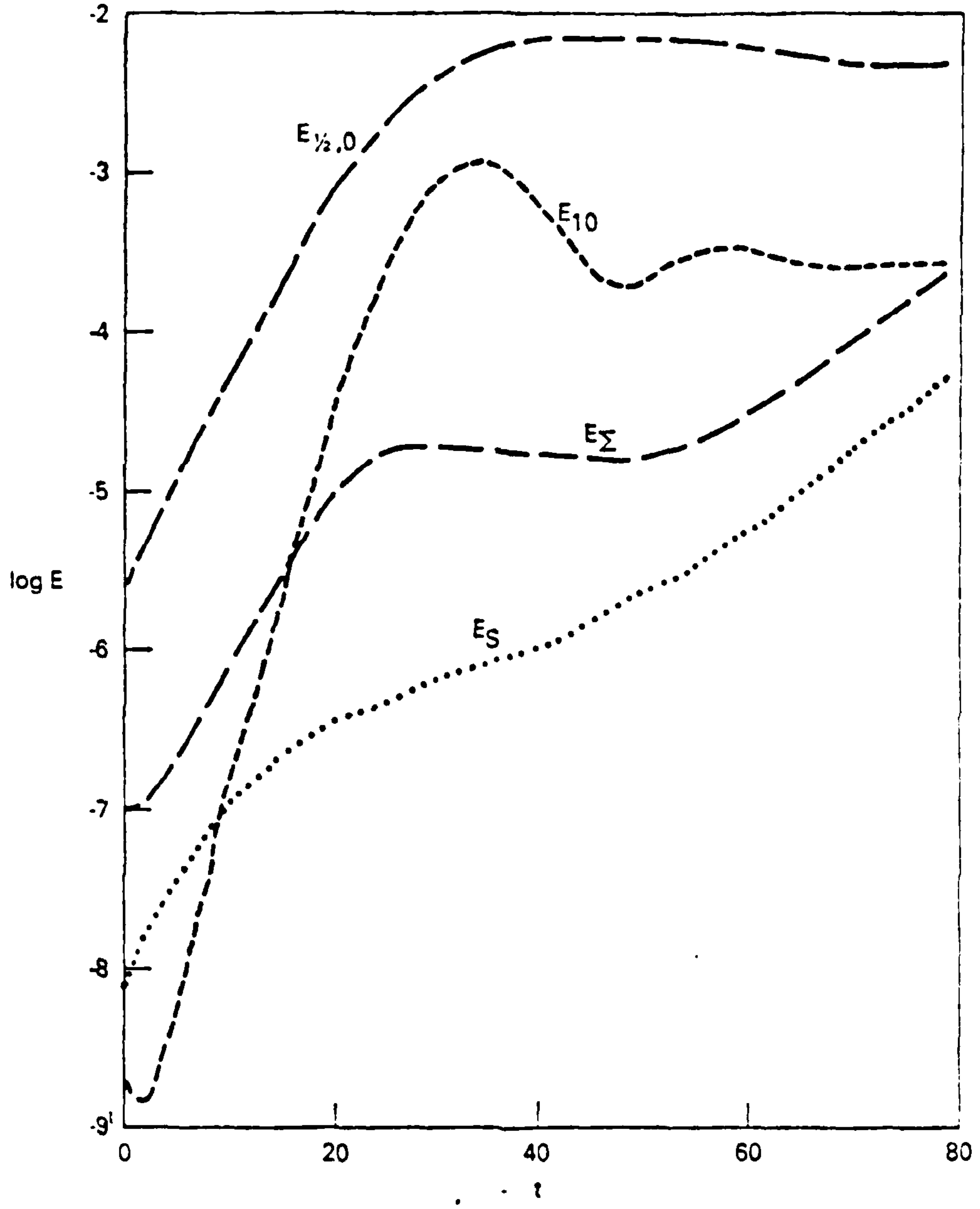

Fig. 17

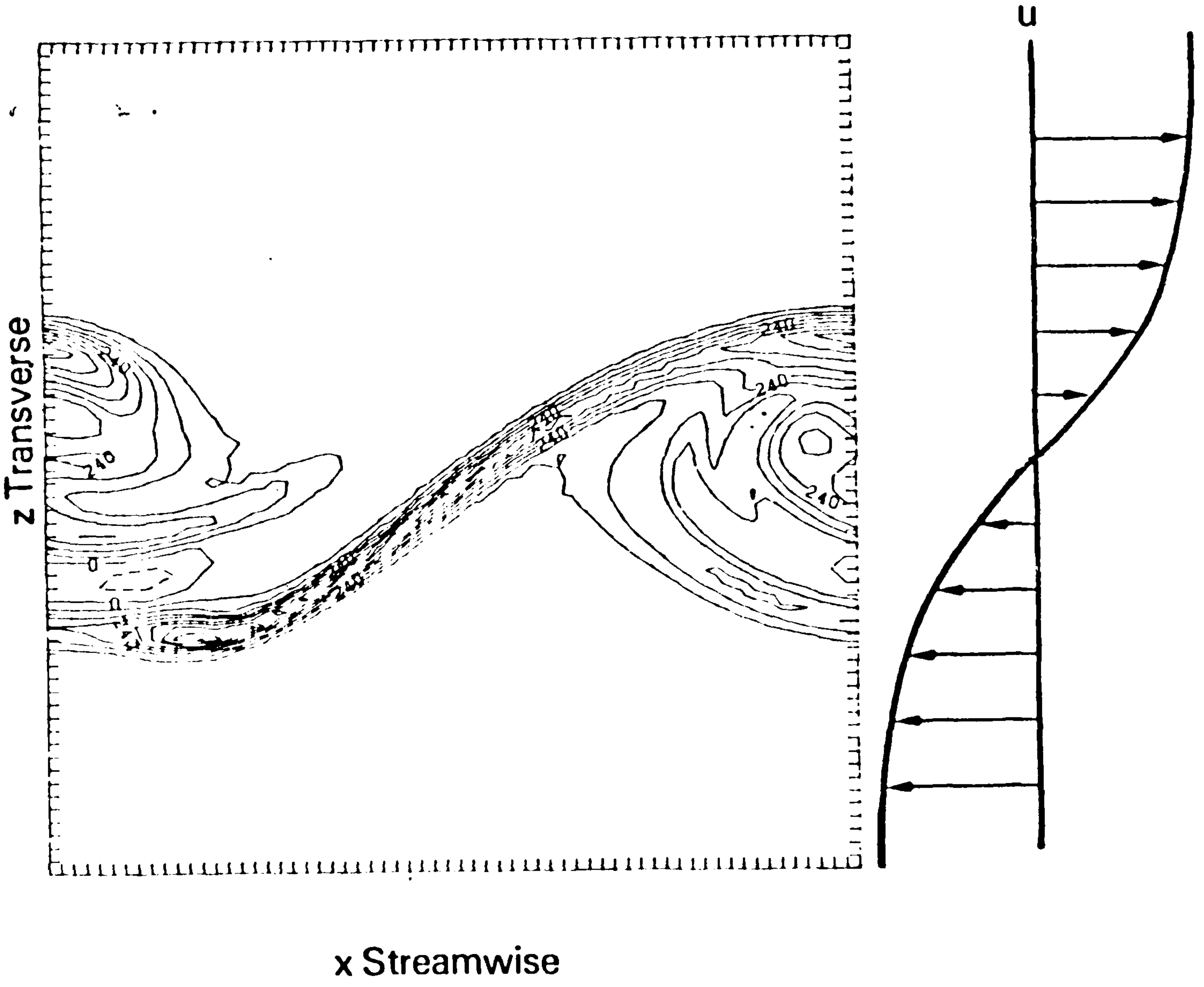

Fig. 18a

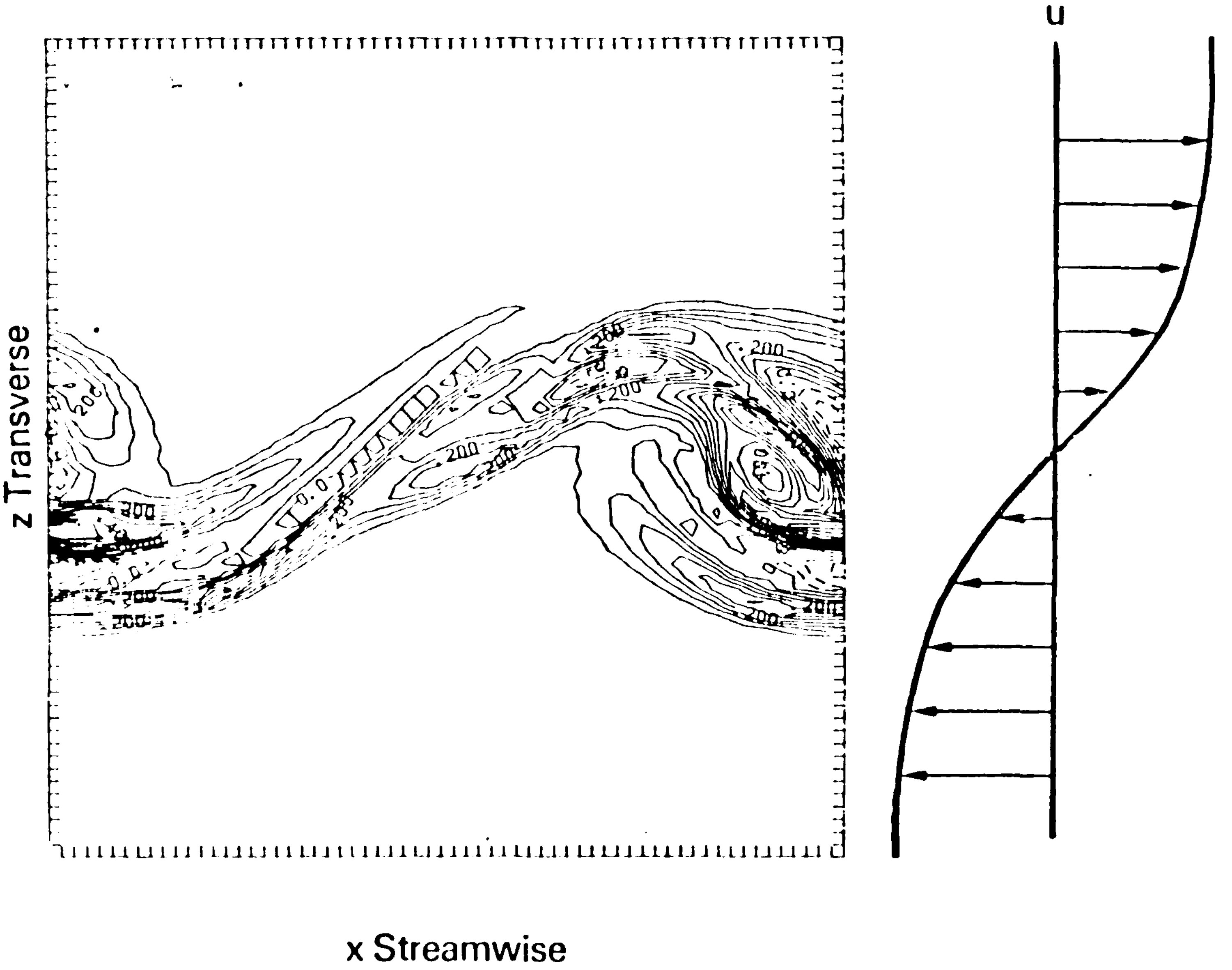

Fig. 18b

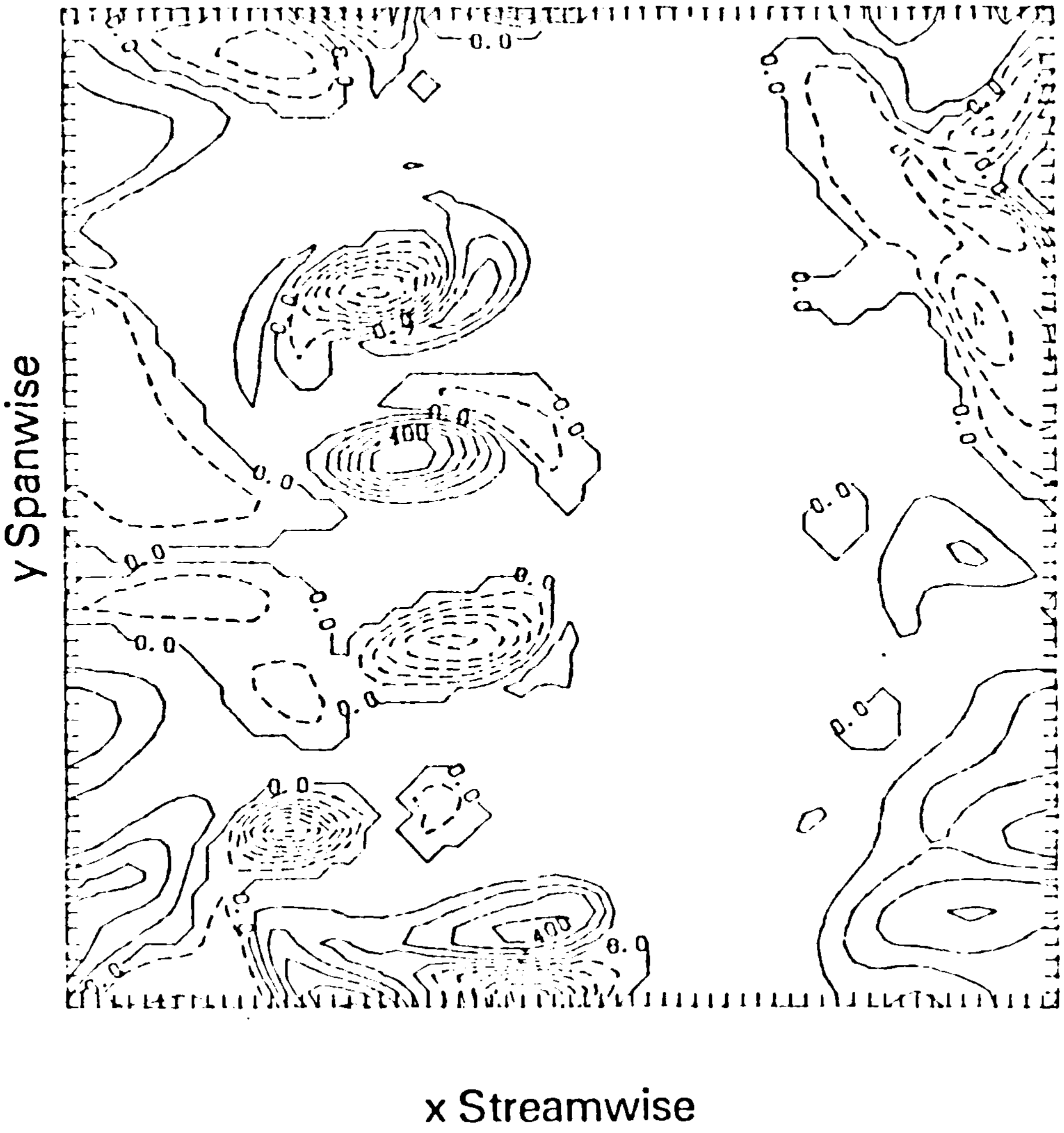

Fig. 19

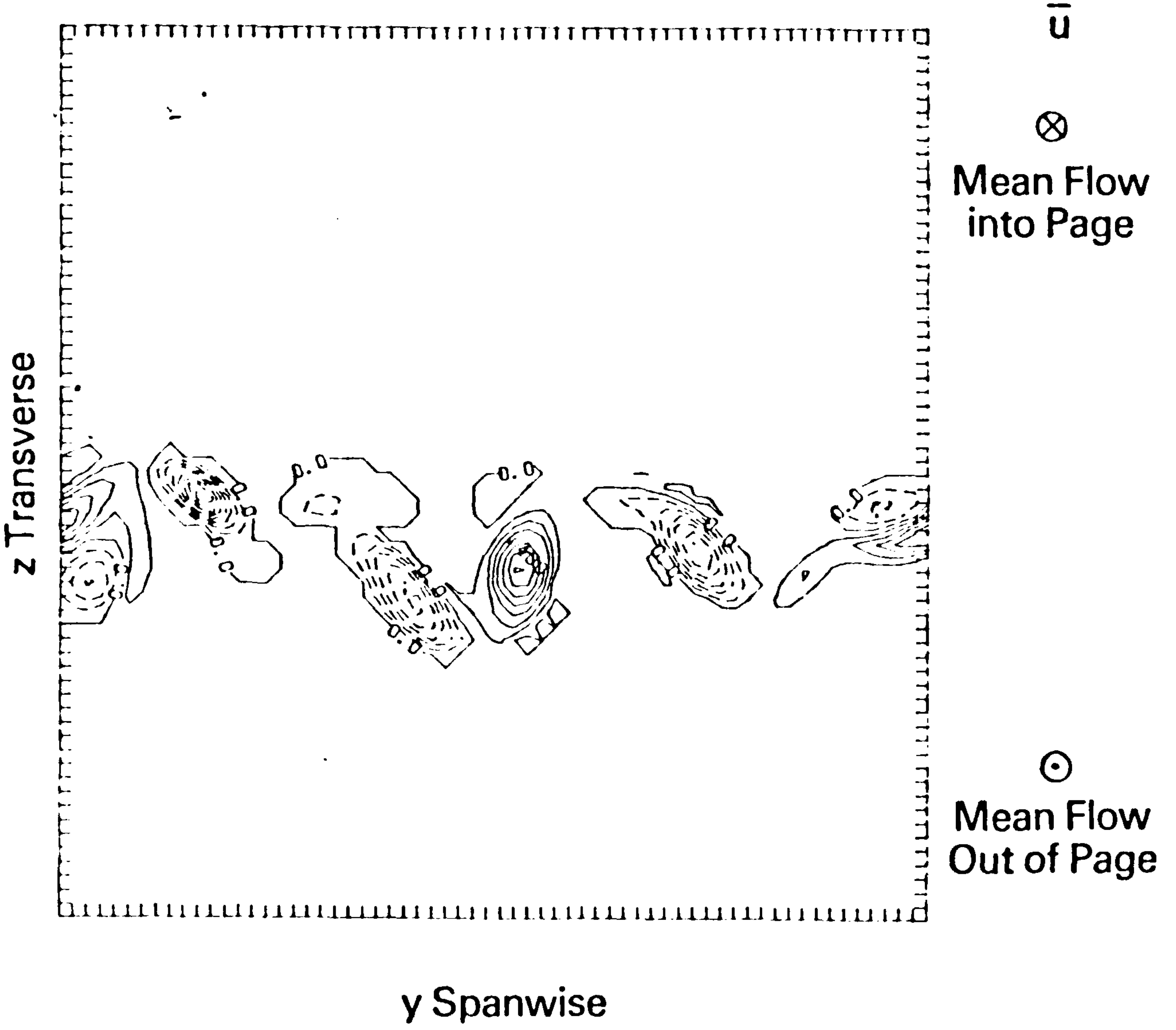
$\bar{u}$
⊗ Mean Flow into Page
⊙ Mean Flow Out of Page
z Transverse
y Spanwise
0.0
0.0
0.0
0.0

Fig. 20

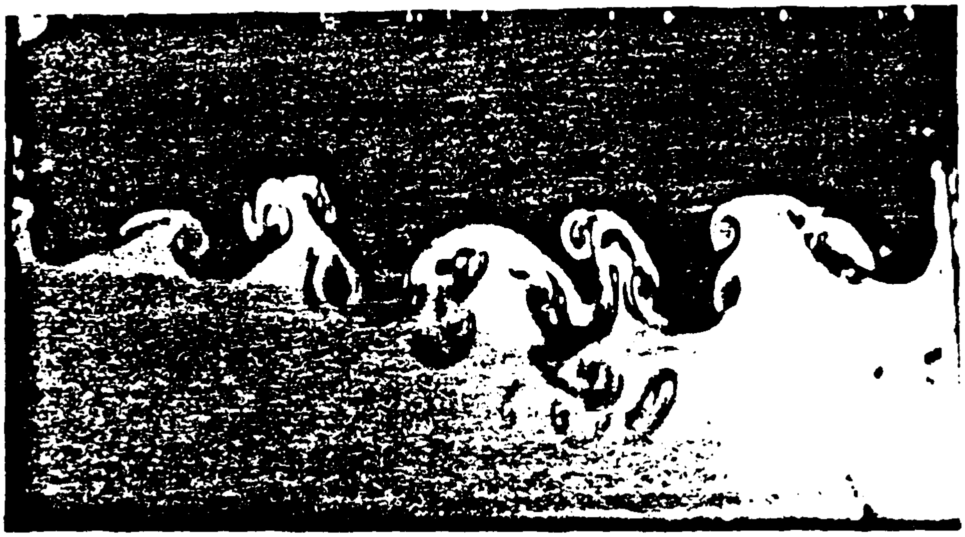

Fig. 21a

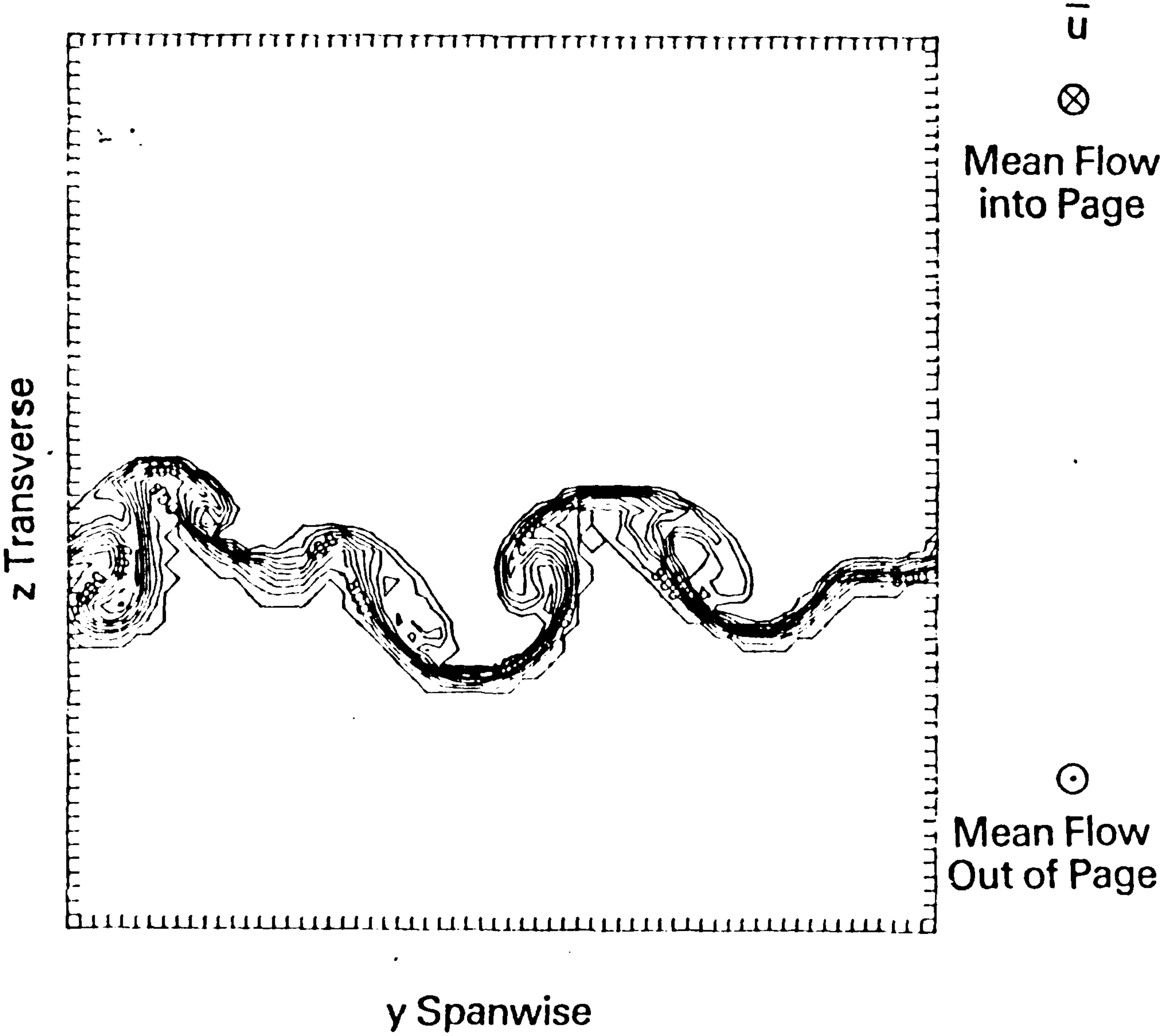
$\bar{u}$
⊗
Mean Flow into Page
⊙
Mean Flow Out of Page
z Transverse
y Spanwise

Fig. 21b

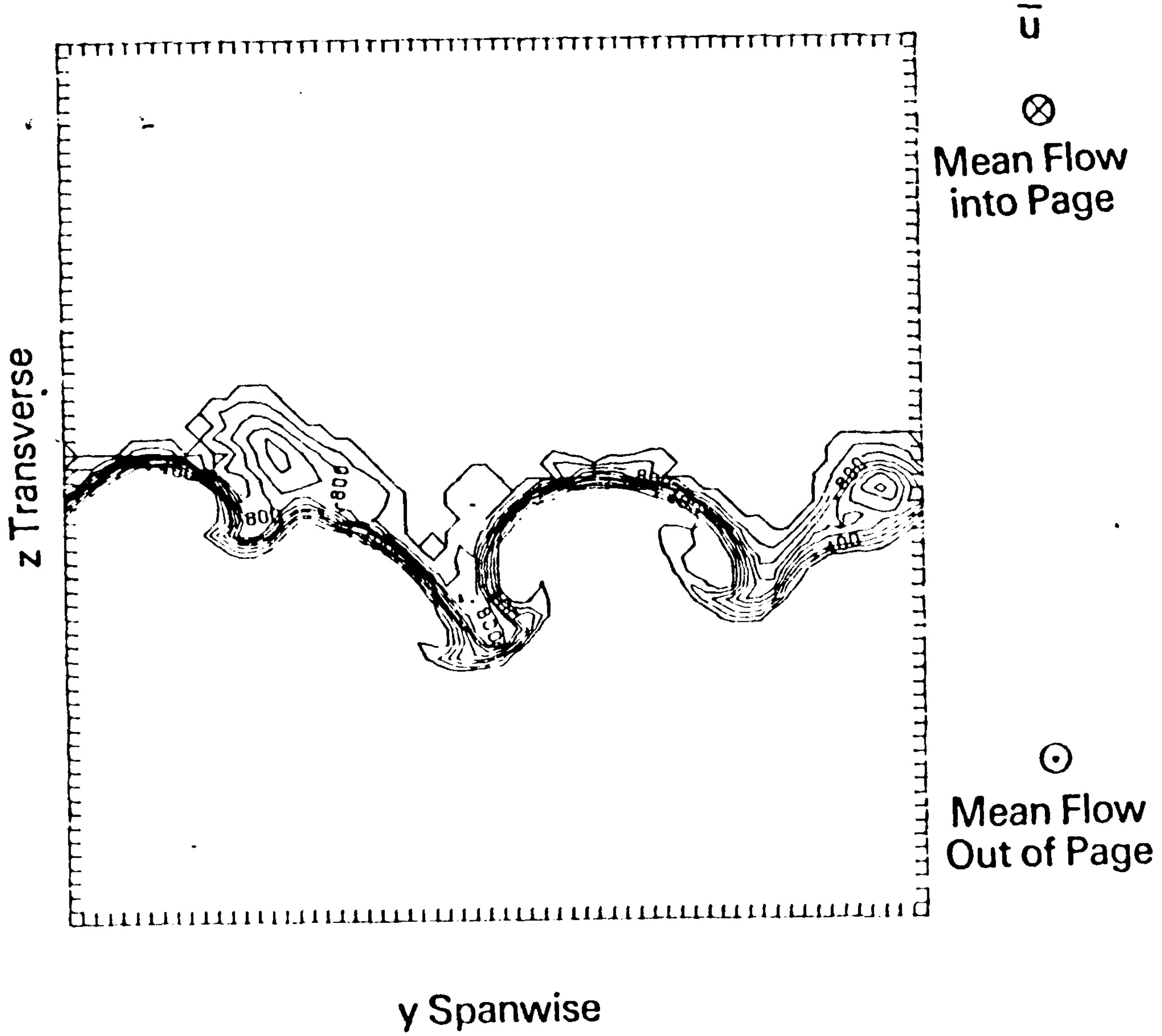
$\bar{u}$
⊗
Mean Flow into Page
⊙
Mean Flow Out of Page
z Transverse
y Spanwise
800
800
800
400
880

Fig. 21c

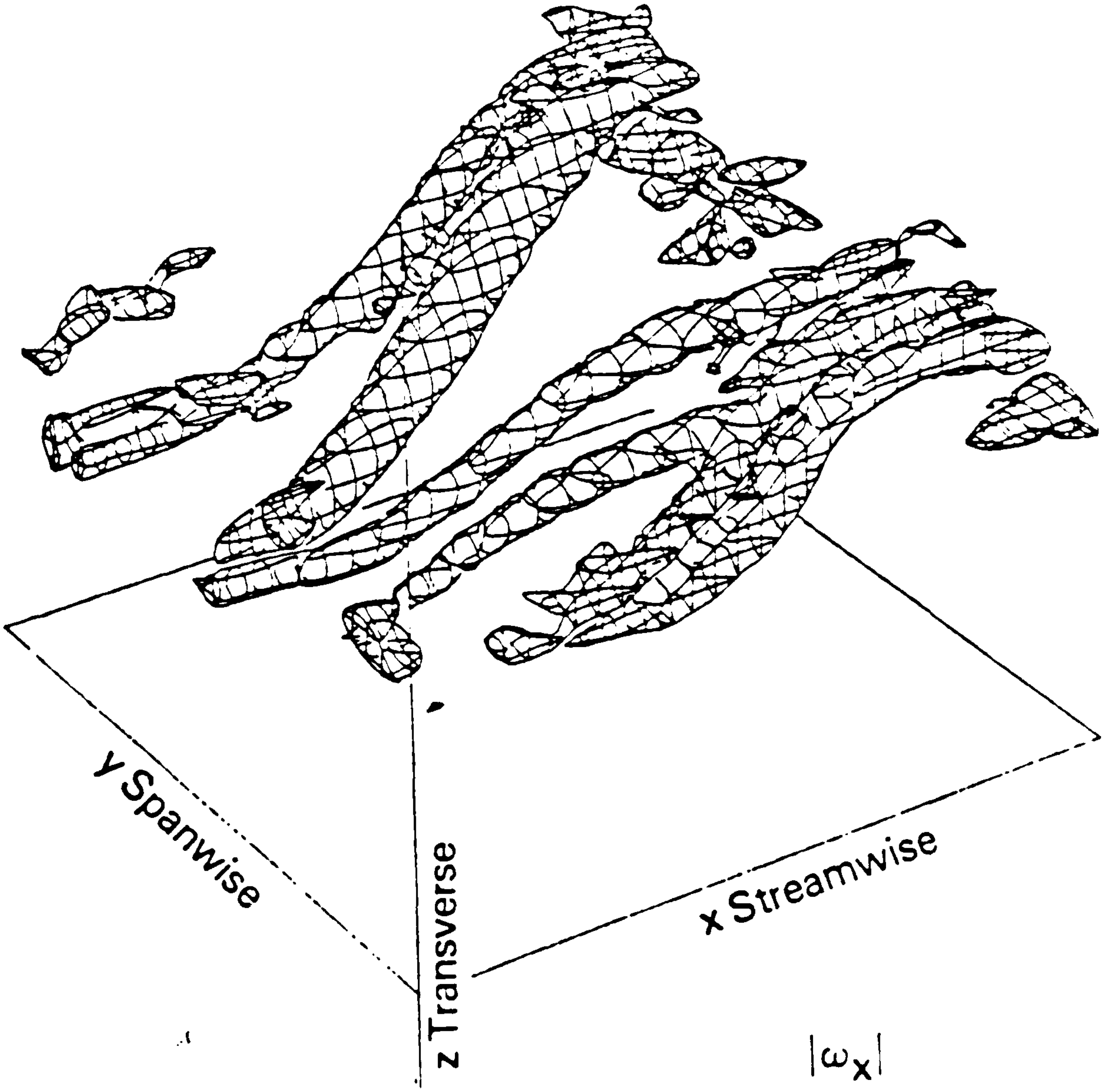
y Spanwise
z Transverse
x Streamwise
$|\omega_x|$

Fig. 22

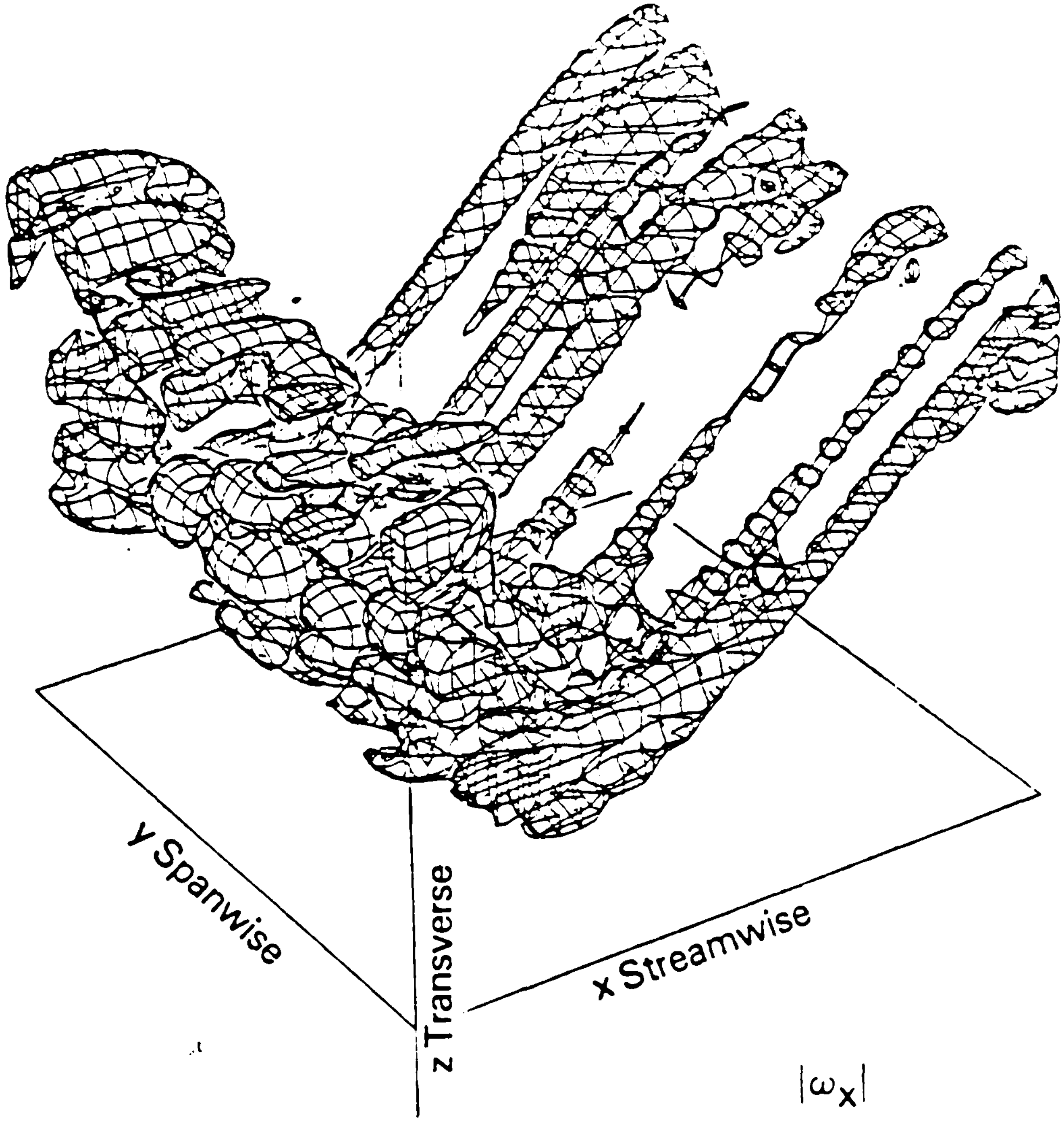
y Spanwise
z Transverse
x Streamwise
$|\omega_x|$

Fig. 23

END
11-87
DTIC